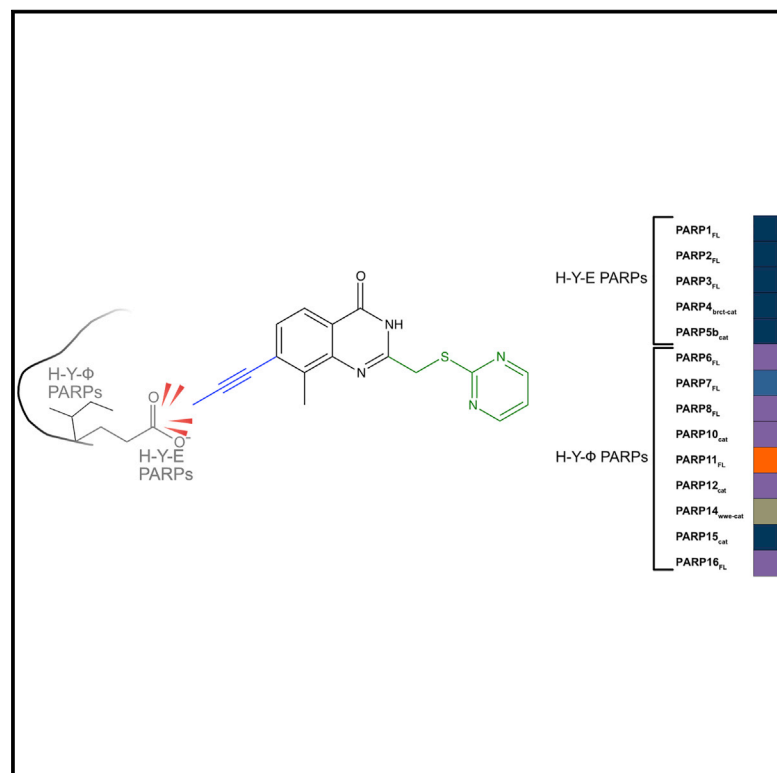


Cell Chemical Biology

A Potent and Selective PARP11 Inhibitor Suggests Coupling between Cellular Localization and Catalytic Activity

Graphical Abstract



Authors

Ilsa T. Kirby, Ana Kojic,
Moriah R. Arnold, ..., Carsten Schultz,
Herwig Schöler, Michael S. Cohen

Correspondence

cohenmic@ohsu.edu

In Brief

Kirby et al. use a structure-guided design strategy to develop a selective and potent inhibitor of PARP11. Cellular studies using this inhibitor revealed the surprising finding that PARP11 nuclear envelope localization is linked to its catalytic activity. This inhibitor will be useful for unraveling the cellular roles of PARP11.

Highlights

- Structure-guided design of PARP inhibitors
- Identification of a potent and selective PARP11 inhibitor (ITK7)
- ITK7 inhibits PARP11 auto-MARylation in cells
- ITK7 causes PARP11 to dissociate from the nuclear envelope

A Potent and Selective PARP11 Inhibitor Suggests Coupling between Cellular Localization and Catalytic Activity

Ilsa T. Kirby,^{1,2} Ana Kojic,^{3,4} Moriah R. Arnold,² Ann-Gerd Thorsell,⁵ Tobias Karlberg,⁵ Anke Vermehren-Schmaedick,² Raashi Sreenivasan,² Carsten Schultz,^{1,2,3} Herwig Schöler,⁵ and Michael S. Cohen^{1,2,6,*}

¹Program in Chemical Biology, Oregon Health & Science University, Portland, OR 97210, USA

²Department of Physiology and Pharmacology, Oregon Health & Science University, Portland, OR 97210, United States

³European Molecular Biology Laboratory (EMBL), Cell Biology and Biophysics Unit, Meyerhofstrasse 1, 69117 Heidelberg, Germany

⁴EMBL, Heidelberg University, Heidelberg, Germany

⁵Department of Biosciences and Nutrition, Karolinska Institutet, Hälsovägen 7c, 14157, Huddinge, Sweden

⁶Lead Contact

*Correspondence: cohenmic@ohsu.edu

<https://doi.org/10.1016/j.chembiol.2018.09.011>

SUMMARY

Poly-ADP-ribose polymerases (PARPs1-16) play pivotal roles in diverse cellular processes. PARPs that catalyze poly-ADP-ribosylation (PARylation) are the best characterized PARP family members because of the availability of potent and selective inhibitors for these PARPs. There has been comparatively little success in developing selective small-molecule inhibitors of PARPs that catalyze mono-ADP-ribosylation (MARylation), limiting our understanding of the cellular role of MARylation. Here we describe the structure-guided design of inhibitors of PARPs that catalyze MARylation. The most selective analog, ITK7, potently inhibits the MARylation activity of PARP11, a nuclear envelope-localized PARP. ITK7 is greater than 200-fold selective over other PARP family members. Using live-cell imaging, we show that ITK7 causes PARP11 to dissociate from the nuclear envelope. These results suggest that the cellular localization of PARP11 is regulated by its catalytic activity.

INTRODUCTION

Poly-ADP-ribose polymerases (PARPs1-16) are key regulators of diverse cellular processes, including DNA repair, transcription, the unfolded protein response, and RNA processing (Gupte et al., 2017). PARPs catalyze ADP-ribosylation, which involves the transfer of ADP-ribose from nicotinamide adenine dinucleotide (NAD⁺) to amino acids in proteins. Active PARPs can be divided into two subfamilies based on a shared active site triad motif: the H-Y-E PARPs (PARP1-4, 5a, and 5b) and the H-Y-Φ PARPs (PARP 6-8, 10-12, and 14-16) (Hottiger et al., 2010). The glutamate in the H-Y-E motif is necessary for the poly-ADP-ribosylation (PARylation) activity of several H-Y-E PARPs (Marsischky et al., 1995; Rolli et al., 1997). In contrast, the H-Y-Φ PARPs contain a hydrophobic (Φ) amino acid in the third

position of the triad. Recently, all H-Y-Φ PARPs were shown to catalyze mono-ADP-ribosylation (MARylation) (Vyas et al., 2014). Unlike H-Y-E PARPs, H-Y-Φ PARPs remain largely uncharacterized.

Selective inhibitors of PARP1,2 (e.g., veliparib) (Donawho et al., 2007) have validated the roles for these PARPs in the DNA damage response pathway. Likewise, selective inhibitors of PARP5a,b (AZ6102) (Johannes et al., 2015) demonstrated roles for PARP5a,b in Wnt signaling (Huang et al., 2009). Similar to selective inhibitors of H-Y-E PARPs, selective inhibitors of individual H-Y-Φ PARPs would be useful in elucidating the function of MARylation. Unfortunately, the dearth of inhibitors that potently and selectively inhibit the H-Y-Φ PARP subfamily has hindered our understanding of H-Y-Φ PARPs (Wahlberg et al., 2012). Recent studies demonstrate that H-Y-Φ PARPs (e.g., PARP14) are therapeutic targets for several cancers (Barbarulo et al., 2013; Iansante et al., 2015) as well as allergic asthma (Mehrotra et al., 2013), highlighting the need to develop selective inhibitors of H-Y-Φ PARPs.

Thus far, the only published small-molecule inhibitors targeting H-Y-Φ PARPs are against PARP10 (e.g., OUL35) (Ekblad et al., 2015; Venkannagari et al., 2016) and PARP14 (Ekblad et al., 2015; Peng et al., 2016; Upton et al., 2017; Yoneyama-Hirozane et al., 2017). While OUL35 was shown to be selective for PARP10 over several other PARP family members, the recently described PARP14 are either not selective over H-Y-E PARPs or their selectivity has not been fully determined. One major challenge in developing inhibitors of H-Y-Φ PARPs is identifying compounds that do not inhibit H-Y-E PARPs yet are potent enough to be used in cellular studies. Here we describe a structure-guided approach for developing small-molecule inhibitors designed to exploit unique features found in H-Y-Φ PARPs. This strategy led to a selective, cell-active small-molecule inhibitor of PARP11.

RESULTS

Structure-Guided Design Leads to Small Molecule Inhibitors Selective for H-Y-Φ PARPs

We sought to identify amino acid differences in the active site between H-Y-E PARPs and H-Y-Φ PARPs that we could exploit for inhibitor design. One major difference between H-Y-E PARPs

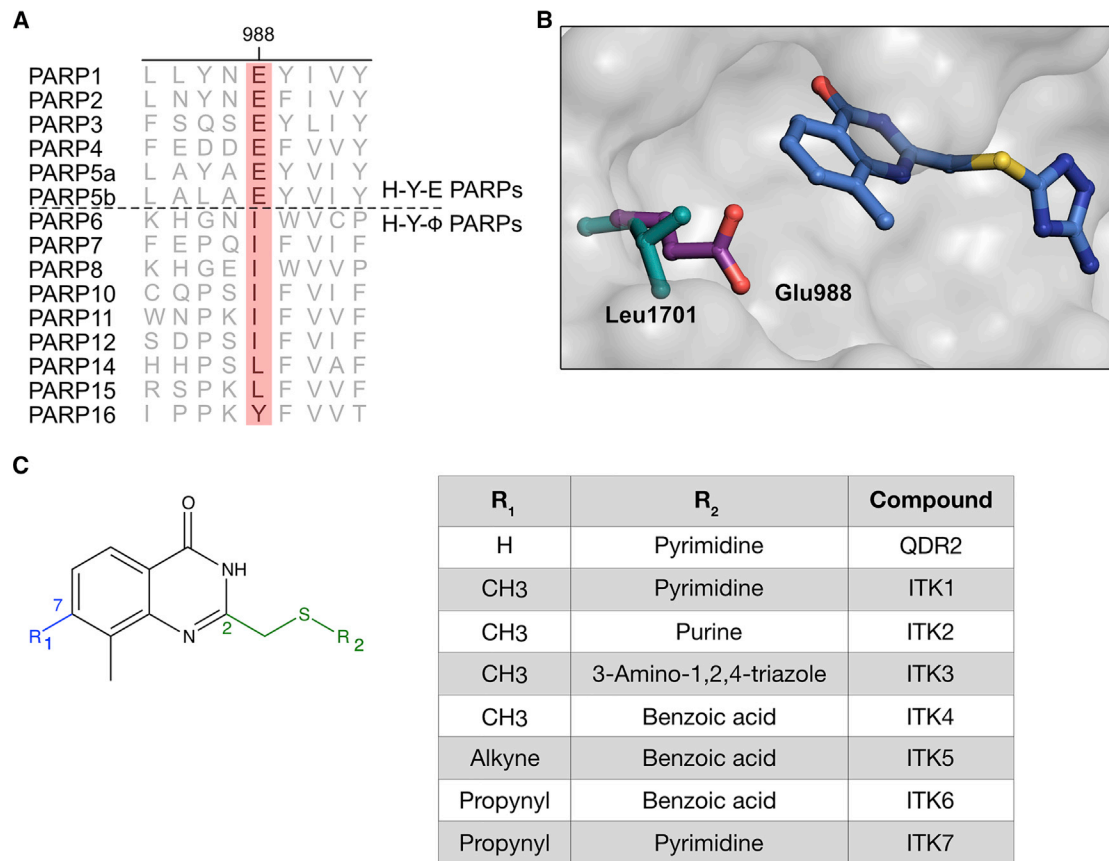


Figure 1. Structure-Guided Design of Selective H-Y-Φ PARP Inhibitors

(A) Structure-based sequence alignment of the PARPs. PARylating PARPs contain a glutamate (Glu988, human PARP1 numbering) in the third position of the H-Y-E triad, while MARylating PARPs contain a hydrophobic (Φ) amino acid at this position.

(B) The crystal structure of QDR1 bound to the catalytic domain of PARP14 (PDB: 3SMI) shows that substituents at the C-7 position of the QDR scaffold would clash with the glutamate (purple) in the third position of the H-Y-E triad but interact favorably with hydrophobic amino acids in the third position (Leu1701, teal) of the H-Y-Φ triad.

(C) Chemical structure of QDR-based inhibitors described in this study.

and H-Y-Φ PARPs is the identity of the amino acid at the third position in the triad motif (position 988, human PARP1 numbering, Figure 1A). We reasoned that the major difference (i.e., acidic versus hydrophobic) in the amino acid at the third position of the conserved triad could potentially be exploited for the development of selective inhibitors of H-Y-Φ PARPs.

To this end, we needed an appropriate scaffold as a starting point for H-Y-Φ PARP-selective inhibitors. We scrutinized the structure of a pan-PARP inhibitor with a quinazolin-4(3H)-one scaffold (QDR1) bound to the nicotinamide binding site of PARP14 (Wahlberg et al., 2012). By overlaying the PARP14-QDR1 structure with that of PARP1 we hypothesized that small, aliphatic substituents at the C-7 position of the QDR scaffold would interact favorably with hydrophobic amino acids (Φ) in the third position of H-Y-Φ PARPs, but would sterically clash with the glutamic acid in H-Y-E PARPs (Figures 1B and 1C).

To test this hypothesis, we synthesized a QDR-based compound with a methyl group at the C-7 position and the des-methyl version (ITK1 and QDR2, Figure 1C; Data S2 [Scheme S1]). We initially tested ITK1 and QDR2 against the well-characterized H-Y-E PARPs PARP1 and PARP2 (Figures 2 and S1;

Table S1) using histones as protein substrates and a clickable NAD⁺ analog to monitor ADP-ribosylation *in vitro* (Carter-O'Connell et al., 2014; Morgan et al., 2015). QDR2 was moderately potent against PARP1 (half maximal inhibitory concentration [IC₅₀] = 1.3 μM) and PARP2 (IC₅₀ = 0.8 μM), while ITK1 only weakly inhibited PARP2 (IC₅₀ = 17.4 μM) and did not inhibit PARP1 at concentrations up to 30 μM. ITK1 did not inhibit PARP3 or the catalytic domain of PARP5b (PARP5b_{cat}) at concentrations up to 10 μM. Thus, the replacement of a hydrogen atom for a methyl group at the C-7 position of the QDR scaffold decreases potency against H-Y-E PARPs.

We next determined if ITK1 inhibited H-Y-Φ PARPs, and if it was more potent than the des-methyl analog QDR2. We note that for several PARPs used for these assays, the catalytic domain alone or a combination with another domain was used because of our inability to generate, in *E. coli*, sufficient quantity and purity of several of the full-length PARPs. We focused initially on the H-Y-Φ PARP PARP14 because our structural analysis was based on the crystal structure of PARP14 bound to QDR1. We tested ITK1 against PARP14 containing the catalytic and WWE domains (PARP14_{cat-wwe}) (Figure S1) using the promiscuous H-Y-Φ PARP

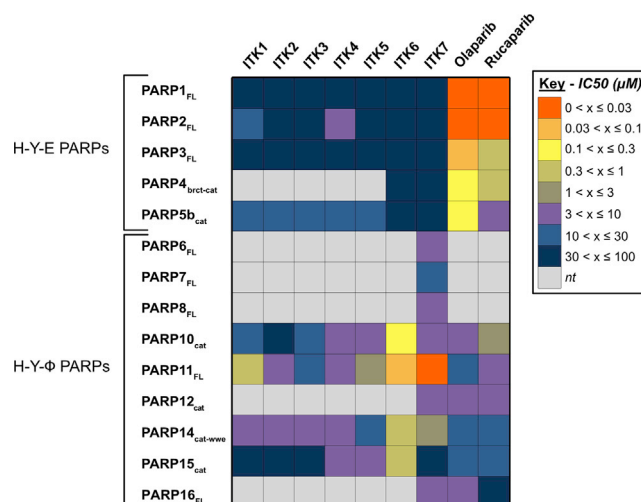


Figure 2. Inhibitor Screen across the PARP Family

Heatmap depicting the IC₅₀ values determined for the ITK series, olaparib, and rucaparib against the PARPs. Values based on at least three replicates.

substrate SRSF protein kinase 2 (SRPK2) (Morgan et al., 2015; Venkannagari et al., 2013). We found that ITK1 was 2-fold more potent than QDR2 against PARP14_{cat-wwe} (IC₅₀ = 8.6 versus 16 μM) (Figures 2 and S1; and Table S1). ITK1 also exhibited moderate potency against the H-Y-Φ PARPs PARP10_{cat} and PARP15_{cat}, and sub-micromolar potency against PARP11. This suggests that modification at the C-7 position is a promising approach toward selectively inhibiting H-Y-Φ PARPs but not H-Y-E PARPs.

Structural Studies of ITK1 Reveal a Hydrophobic Sub-pocket in an H-Y-Φ PARP

We next solved the crystal structure of ITK1 bound to PARP14_{cat}. PARP14 was used for structural studies so we could directly compare the PARP14-ITK1 structure with the previously determined PARP14-QDR1 structure. Comparing the PARP14-ITK1 structure with the PARP14-QDR1 structure revealed that Leu1701 rotates toward the methyl group at the C-7 position of QDR2 (Figure 3A). The C-7 methyl group also points toward a hydrophobic sub-pocket lined by Leu1701, Val1626, Ala1627, and Tyr1628 at the C terminus of the donor loop (D-loop) (Figure 3A). The D-loop—a flexible loop that abuts the NAD⁺ binding site—is one of the least conserved elements in the PARP catalytic domains (Figure 3B) (Pinto and Schüler, 2015). While the exact function of the D-loop is unclear, studies of related bacterial toxins suggest its involvement in NAD⁺ binding (Jørgensen et al., 2005, 2008). While structural comparison of various H-Y-Φ PARPs highlight D-loop flexibility, the hydrophobic sub-pocket appears to be a static feature of H-Y-Φ PARPs (Wahlberg et al., 2012). The hydrophobic sub-pocket is sterically occluded by the glutamate in H-Y-E PARPs and could potentially serve as a selectivity filter within the H-Y-Φ PARP active site.

Exploiting Differences in the D-Loop to Discriminate among H-Y-Φ PARPs

In the PARP14-ITK1 structure the N-terminal region of the PARP14 D-loop interacts with the pyrimidine substituent at the

C-2 position of ITK1 (Figure 3C). Given the lack of sequence conservation within the D-loop of H-Y-Φ PARPs we envisaged that modifications at this position could result in selective inhibition of individual H-Y-Φ PARP family members. We synthesized three C-7 methyl QDR analogs with various substituents at C-2 (ITK2, adenosine; ITK3, 3-amino-triazole; ITK4, *p*-benzoic acid) (Figure 1C; Data S2 [Scheme S1]). We screened these compounds against the H-Y-E PARPs (PARP1-3 and PARP5b_{cat}) and the H-Y-Φ PARPs (PARP10_{cat}, PARP11, PARP14_{cat-wwe}, and PARP15_{cat}) (Figure 2 and S1; Table S1). None of these QDR analogs inhibited PARPs 1-3 or 5b_{cat} (up to 30 and 10 μM, respectively) except ITK4, which modestly inhibited PARP2 (IC₅₀ = 8.5 μM). Therefore, the methyl substituent at C-7 decreases binding of QDR analogs to H-Y-E PARPs. Among the H-Y-Φ PARPs, ITK2-4 did not exhibit improved potency or selectivity over ITK1. This indicates that selectivity for PARP11 can be achieved with a pyrimidine at the C-2 position of the QDR scaffold. This selectivity is likely due to specific interactions between the pyrimidine and amino acids in the D-loop of PARP11.

Further Modification of the C-7 Position of the QDR Scaffold Improves Potency

We hypothesized that modification at the C-7 position with a larger substituent would yield increases in potency by extending further into the hydrophobic sub-pocket. We synthesized two compounds containing either an alkynyl (ITK5) or a propynyl (ITK6) substituent at the C-7 position and a *p*-benzoic acid at the C-2 position (Figure 1; Data S2 [Scheme S2]). Compared with ITK4, ITK6 exhibited substantially improved potency against PARP10_{cat} (60-fold) and PARP11 (55-fold), while modestly improving potency against PARP14_{cat-wwe} (10-fold) and PARP15_{cat} (15-fold). Importantly, ITK6 did not inhibit PARP1-4 and PAR5b up to 30 μM. We obtained a crystal structure of ITK6 bound to the catalytic domain of PARP14, which confirmed that the propynyl substituent projects further into the hydrophobic sub-pocket (Figure 3D). These results show that targeting the hydrophobic sub-pocket found in the H-Y-Φ PARPs is a viable strategy for the development for H-Y-Φ PARP-selective inhibitors.

Design of a Potent and Selective PARP11 Inhibitor

The structure-activity relationship study exploring the C-2 position of the QDR scaffold demonstrated that the pyrimidine at the C-2 position of ITK1 yielded selectivity for PARP11 (Figure 2; Table S1). We reasoned that replacing the C-7 methyl in ITK1 with a propynyl group (ITK7, Figure 1; Data S2 [Scheme S2]) would yield a more potent and selective PARP11 inhibitor. Indeed, we found that ITK7 potently inhibited PARP11 (IC₅₀ = 14 nM), and with greater than 200-fold selectivity over other H-Y-Φ PARPs, while not inhibiting any of the H-Y-E PARPs (Figures 2 and S1; Table S1). ITK7 exhibited similar potency against PARP11 using nuclear export factor 1, a previously identified cellular target of PARP11 (Carter-O'Connell et al., 2016), as a substrate instead of the pan-substrate SRPK2 (Figure S1C). Furthermore, ITK7 exhibited similar potency against PARP11 when native NAD⁺ was used instead of 6-a-NAD⁺ (Figure S1). Compared with two US Food and Drug Administration-approved drugs, olaparib and rucaparib (Bitler et al., 2017; Menear et al., 2008; Thomas et al., 2007), which potently inhibit several H-Y-E PARPs (Thorsell et al., 2017; Wahlberg et al., 2012), and

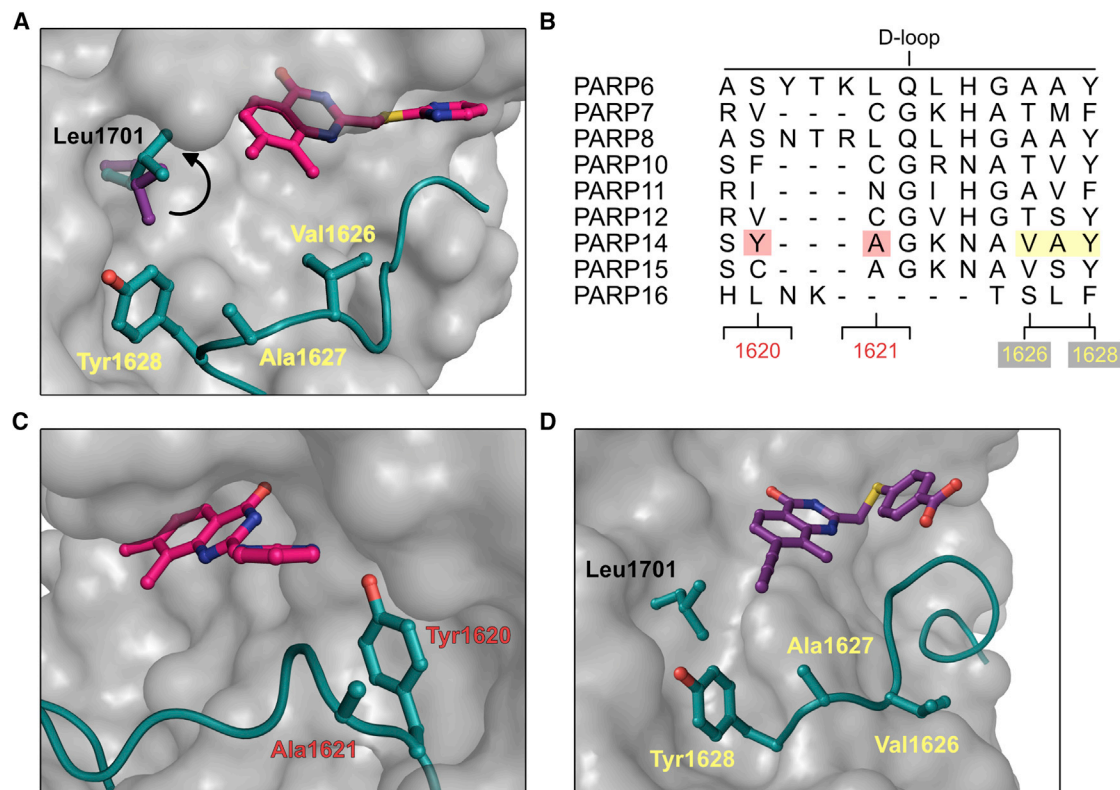


Figure 3. Exploiting a Hydrophobic Sub-pocket in H-Y- Φ PARPs with C-7-Substituted QDR Analogs

(A) Crystal structure of ITK1 (magenta) (PDB: 6FYM) bound to PARP14_{cat}. Leu1701 rotates toward the C-7 methyl group of ITK1 to make hydrophobic contacts compared with its position bound to QDR1 (violet, Leu1701 in the QDR1 bound structure; teal, Leu1701 in ITK1 bound structure). The C-7 methyl group of ITK1 projects into a hydrophobic sub-pocket formed by Leu1701 and amino acids located at the C terminus of the D-loop.

(B) Structure-based sequence alignment showing the amino acids in the D-loop. Tyr1620 and Ala1621 in PARP14 are highlighted in pink, Val1626, Ala1627, and Tyr1628 in PARP14 are highlighted in yellow.

(C) Interactions between the amino acids (Ala1621 and Tyr1620, in particular) in the N terminus of the D-loop (teal) and the C-2 substituent of ITK1.

(D) Crystal structure of ITK6 (violet) (PDB: 6FZM) bound to PARP14_{cat}. The propynyl substituent at the C-2 position of ITK6 occupies the hydrophobic sub-pocket.

modestly inhibit a few H-Y- Φ PARPs (Figure 2; Table S1), ITK7 is one of the most potent and selective PARP inhibitors described to date.

ITK7 Inhibits PARP11 Auto-MARylation Activity in Cells and Causes PARP11 to Dissociate from the Nuclear Envelope

We next examined the effects of ITK7 on PARP11 activity in cells. Similar to other PARPs, PARP11 undergoes auto-MARylation (Carter-O'Connell et al., 2016; Vyas et al., 2014). Because there are no validated cell-based assays for examining endogenous PARP11 activity or function, we used HeLa cells expressing full-length GFP-PARP11 to test ITK7. HeLa cells were treated with increasing concentrations of ITK7 for 3 hr (Figure 4A). ITK7 exhibited a dose-dependent inhibition of PARP11-dependent auto-MARylation (EC_{50} = 13 nM) (Figures 4A and 4B). Importantly, ITK7 did not inhibit H_2O_2 -activated PARP1 auto-PARylation (Figure S2A). Unlike our pan-H-Y- Φ PARP inhibitor ITK6, ITK7 did not inhibit PARP10 auto-MARylation in cells (Figures S2B and S2C), further demonstrating the specificity of ITK7 for PARP11.

We and others have demonstrated that PARP11 localizes to the nuclear envelope (Carter-O'Connell et al., 2016; Meyer-Ficca

et al., 2015) and MARylates several nuclear pore complex (NPC) proteins in HEK293T cells (Carter-O'Connell et al., 2016). Here, we confirmed that GFP-PARP11 localizes to the nuclear envelope, where it colocalizes with an mRuby2-tagged NPC protein NUP50 in HeLa cells (Figure S3A). A previous study showed that PARP11 nuclear envelope localization requires the presence of the catalytic domain (Meyer-Ficca et al., 2015). Similarly, we found that a GFP-tagged PARP11 mutant with severely compromised catalytic activity—I313G (IG) GFP-PARP11 (Carter-O'Connell et al., 2016)—exhibited substantially reduced nuclear envelope localization compared with wild-type GFP-PARP11 (Figure 4C). These results suggest that the catalytic activity of PARP11 is required for nuclear envelope localization.

We next treated GFP-PARP11-transfected HeLa cells with ITK7 (1 μ M) and used live-cell imaging to monitor GFP-PARP11 localization. We found that GFP-PARP11 dissociated from the nuclear pore within 30 min of treatment with ITK7 (1 μ M), while treatment with DMSO had no effect (Figures 4D and 4E; Videos S1 and S2). Upon longer treatment (18 hr), GFP-PARP11 could no longer be detected at the nuclear envelope and appeared to accumulate in the nucleus (Figure S3B). These results support the hypothesis that the catalytic activity of PARP11 is required for localization to the nuclear envelope.

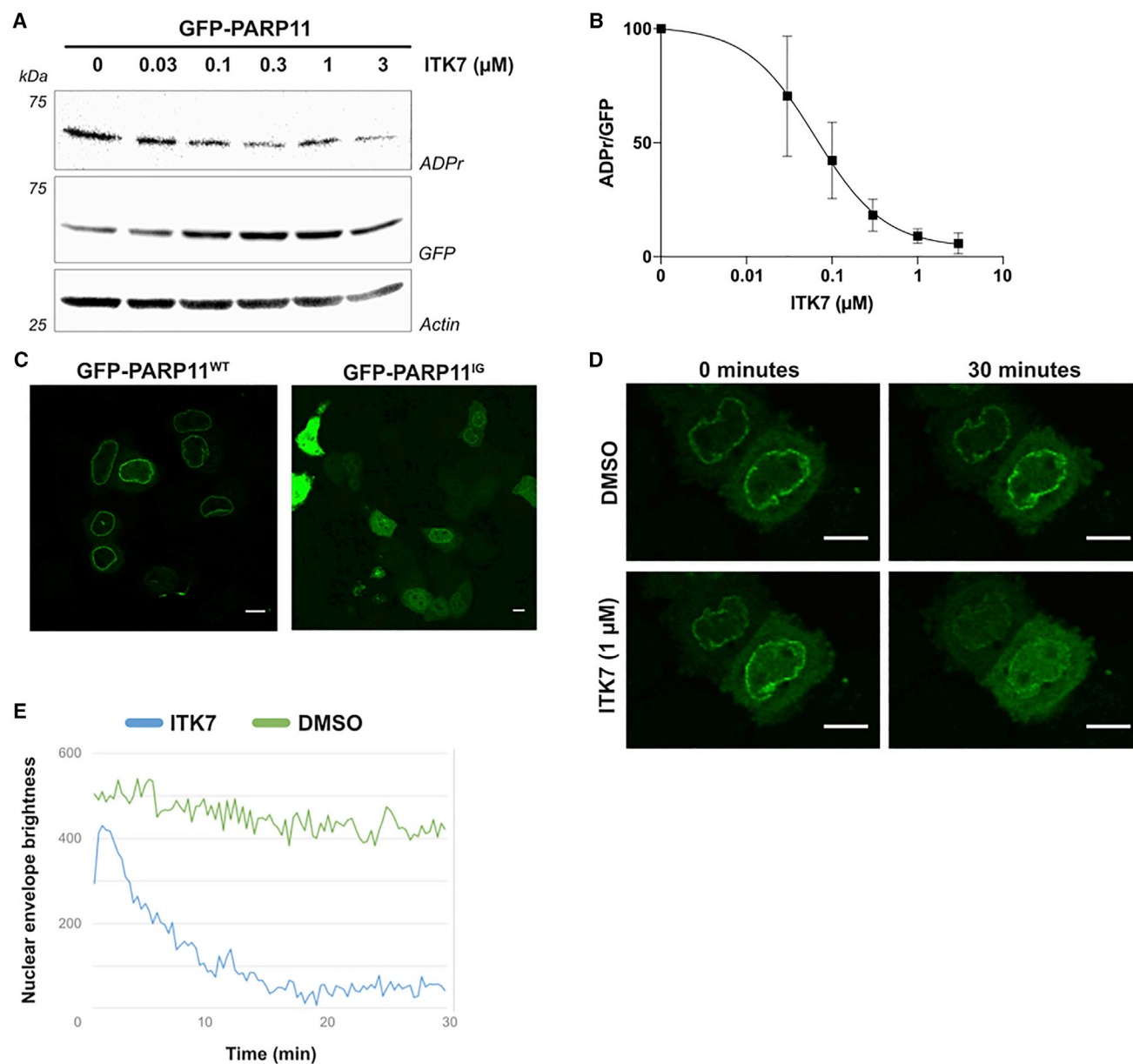


Figure 4. PARP11 Catalytic Activity Is Required for Nuclear Envelope Localization

(A) ITK7 inhibits GFP-PARP11 auto-MARylation activity in a dose-dependent manner in HeLa cells. The signal for PARP11 auto-MARylation does not disappear completely, which is likely due to incomplete removal of MAR on PARP11.

(B) Quantification of results shown in (A). Error bars represent \pm SEM from three replicates (Prism 7).

(C) A catalytically compromised PARP11 mutant (I313G [IG] GFP-PARP11) does not localize to the nuclear envelope. HeLa cells were transfected with either wild-type or IG GFP-PARP11 and imaged 20 hr post-transfection.

(D) Treatment of HeLa cells with ITK7 caused PARP11 to dissociate from the nuclear envelope. HeLa cells transfected with GFP-PARP11 were treated with either ITK7 or DMSO, and images were acquired every 20 s. Scale bars, 10 μ m.

(E) Quantification of results shown in (C).

Related to Videos S1 and S2.

DISCUSSION

Using structure-guided design we developed QDR-based inhibitors that selectively inhibit H-Y- Φ PARPs. Substitution of the C-7 position of the QDR scaffold is an effective strategy to improve potency against H-Y- Φ PARPs and decrease potency against

the H-Y-E PARPs. Our structural studies reveal that inhibitor selectivity is due to the exploitation of a hydrophobic sub-pocket unique to the H-Y- Φ PARPs. Our most potent compound, ITK7, is remarkably selective for PARP11. Future studies will explore the hydrophobic sub-pocket in PARP11 and other H-Y- Φ PARPs to increase the potency and selectivity of our QDR analogs.

This study demonstrates that the selectivity within the H-Y- Φ PARP subfamily can be optimized by varying the substituent emanating from the C-2 position of the QDR scaffold. This is presumably due to differences in the D-loop between H-Y- Φ PARPs as the amino acids in the active site that are oriented toward the C-2 substituent are not conserved across the H-Y- Φ PARP family. Two out of the three amino acids (Ala229 and Val230, human PARP11 numbering) that line the hydrophobic sub-pocket are not well conserved across the H-Y- Φ PARP family (Figure 3B). This lack of conservation within the D-loop will be exploited to improve selectivity for a given H-Y- Φ PARPs in future studies.

We previously demonstrated that PARP11 is a nuclear envelope-localized PARP and modifies several NPC family members (Carter-O'Connell et al., 2016). How PARP11 regulates NPC proteins is unclear. Our work reveals that ITK7 causes PARP11 to dissociate from the envelope within 30 min. Moreover, a catalytically compromised mutant does not localize to the nuclear envelope. This links the catalytic activity of PARP11 to nuclear envelope localization; future studies will focus on understanding how catalytic activity, and in particular auto-MARylation, regulates PARP11 localization. Given that many PARPs exhibit distinct localization patterns in cells (Vyas et al., 2014) it will be interesting to determine if catalytic activity generally regulates PARP localization. These studies will be greatly facilitated by selective and potent inhibitors of individual PARP family members.

STAR★METHODS

Detailed methods are provided in the online version of this paper and include the following:

- KEY RESOURCES TABLE
- CONTACT FOR REAGENT AND RESOURCE SHARING
- EXPERIMENTAL MODEL AND SUBJECT DETAILS
- METHOD DETAILS
 - Cloning
 - Expression and Purification of Human PARP1-3, PARP10_{cat}, PARP15_{cat}, and SRPK2
 - Expression and Purification of Human Full Length PARP11_{FL} and PARP4_{brct-cat}
 - Expression and Purification of Human PARP7_{FL}
 - Expression and Purification of Human PARP14_{cat-ww}
 - Histone H1 Plate Assays
 - SRPK2 Plate Assays
 - NXF1 Plate Assay
 - Auto-modification Plate Assay for PARP4_{brct-cat}
 - Auto-modification Plate Assay for PARP7_{FL}
 - Native NAD⁺ Plate Assay
 - PARP Immunoprecipitation auto-MARylation Activity Assay
 - GFP-PARP10 MARylation in Cells
 - H₂O₂-stimulated H-Y-E PARP Activation
 - GFP-PARP11 auto-MARylation in Cells
 - Imaging Experiments in HeLa Cells
 - Chemical Synthesis
 - Crystallography Studies
- QUANTIFICATION AND STATISTICAL ANALYSIS
- DATA AND SOFTWARE AVAILABILITY

SUPPLEMENTAL INFORMATION

Supplemental Information includes four figures, one table, two videos, and two data files and can be found with this article online at <https://doi.org/10.1016/j.chembiol.2018.09.011>.

ACKNOWLEDGMENTS

We thank members of the Cohen laboratory for many helpful discussions. We thank K. Rodriguez (Cohen lab) for her support in the synthesis of 6-alkyne-NAD⁺. We thank R. Morgan for PARP15_{cat} and PARP10_{cat} used in this study. We thank J. Matthews (University of Oslo) for the GST-PARP7_{FL} plasmid. We thank A. DeBarber and the OHSU Bioanalytical Shared Resource Facility for high-resolution mass spectrometry analysis of our compounds. We thank S. Ferrara for advice regarding synthesis. This work was supported by the Pew Foundation and Startup funds from OHSU (to M.S.C.), the Swedish Research Council, the Swedish Cancer Society, and the Swedish Foundation for Strategic Research (to H.S.), and by TRR186 of the German Research Council (DFG) (to C.S.).

AUTHOR CONTRIBUTIONS

I.T.K. and M.S.C. designed the experiments. I.T.K. synthesized all reported compounds and conducted all experiments with the exceptions of the live-cell imaging performed by A.K. M.R.A. conducted studies using ITK7 in cells. A.-G.T., T.K., and H.S. conducted crystallography studies. A.V.-S. conducted immunoprecipitation assays. R.S. prepared the PARP11 construct for bacterial expression. I.T.K. and M.S.C. wrote the manuscript with input from the other authors.

DECLARATION OF INTERESTS

I.T.K. and M.S.C. are co-inventors on a provisional patent describing the inhibitors in this study.

Received: June 13, 2017

Revised: June 8, 2018

Accepted: September 24, 2018

Published: October 18, 2018

REFERENCES

- Barbarulo, A., Iansante, V., Chaidos, A., Naresh, K., Rahemtulla, A., Franzoso, G., Karadimitris, A., Haskard, D.O., Papa, S., and Bubici, C. (2013). Poly(ADP-ribose) polymerase family member 14 (PARP14) is a novel effector of the JNK2-dependent pro-survival signal in multiple myeloma. *Oncogene* 32, 4231–4242.
- Bitler, B.G., Watson, Z.L., Wheeler, L.J., and Behbakht, K. (2017). PARP inhibitors: clinical utility and possibilities of overcoming resistance. *Gynecol. Oncol.* 147, 695–704.
- Carter-O'Connell, I., Jin, H., Morgan, R.K., David, L.L., and Cohen, M.S. (2014). Engineering the substrate specificity of ADP-ribosyltransferases for identifying direct protein targets. *J. Am. Chem. Soc.* 136, 5201–5204.
- Carter-O'Connell, I., Jin, H., Morgan, R.K., Zaja, R., David, L.L., Ahel, I., and Cohen, M.S. (2016). Identifying family-member-specific targets of mono-ARTDs by using a chemical genetics approach. *Cell Rep.* 14, 621–631.
- Donawho, C.K., Luo, Y., Luo, Y., Penning, T.D., Bauch, J.L., Bouska, J.J., Bontcheva-Diaz, V.D., Cox, B.F., DeWeese, T.L., Dillehay, L.E., et al. (2007). ABT-888, an orally active poly(ADP-ribose) polymerase inhibitor that potentiates DNA-damaging agents in preclinical tumor models. *Clin. Cancer Res.* 13, 2728–2737.
- Ekblad, T., Lindgren, A.E.G., Andersson, C.D., Caraballo, R., Thorsell, A.-G., Karlberg, T., Spjut, S., Linusson, A., Schüller, H., and Elofsson, M. (2015). Towards small molecule inhibitors of mono-ADP-ribosyltransferases. *Eur. J. Med. Chem.* 95, 546–551.
- Gibson, B.A., Conrad, L.B., Huang, D., and Kraus, W.L. (2017). Generation and characterization of recombinant antibody-like ADP-ribose binding proteins. *Biochemistry* 56, 6305–6316.

- Gupte, R., Liu, Z., and Kraus, W.L. (2017). PARPs and ADP-ribosylation: recent advances linking molecular functions to biological outcomes. *Genes Dev.* **31**, 101–126.
- Hottiger, M.O., Hassa, P.O., Lüscher, B., Schüler, H., and Koch-Nolte, F. (2010). Toward a unified nomenclature for mammalian ADP-ribosyltransferases. *Trends Biochem. Sci.* **35**, 208–219.
- Huang, J.Y., Wang, K., Vermehren Schmaedick, A., Adelman, J.P., and Cohen, M.S. (2016). PARP6 is a regulator of hippocampal dendritic morphogenesis. *Sci. Rep.* **6**, 208.
- Huang, S.-M.A., Mishina, Y.M., Liu, S., Cheung, A., Stegmeier, F., Michaud, G.A., Charlat, O., Wiellette, E., Zhang, Y., Wiessner, S., et al. (2009). Tankyrase inhibition stabilizes axin and antagonizes Wnt signalling. *Nature* **461**, 614–620.
- Iansante, V., Choy, P.M., Fung, S.W., Liu, Y., Chai, J.-G., Dyson, J., Del Rio, A., D'Santos, C., Williams, R., Chokshi, S., et al. (2015). PARP14 promotes the Warburg effect in hepatocellular carcinoma by inhibiting JNK1-dependent PKM2 phosphorylation and activation. *Nat. Commun.* **6**, 7882.
- Johannes, J.W., Almeida, L., Barlaam, B., Boriack-Sjodin, P.A., Casella, R., Croft, R.A., Dishington, A.P., Gingipalli, L., Gu, C., Hawkins, J.L., et al. (2015). Pyrimidinone nicotinamide mimetics as selective tankyrase and Wnt pathway inhibitors suitable for in vivo pharmacology. *ACS Med. Chem. Lett.* **6**, 254–259.
- Jørgensen, R., Merrill, A.R., Yates, S.P., Marquez, V.E., Schwan, A.L., Boesen, T., and Andersen, G.R. (2005). Exotoxin A-eEF2 complex structure indicates ADP ribosylation by ribosome mimicry. *Nature* **436**, 979–984.
- Jørgensen, R., Wang, Y., Visschedyk, D., and Merrill, A.R. (2008). The nature and character of the transition state for the ADP-ribosyltransferase reaction. *EMBO Rep.* **9**, 802–809.
- Langelier, M.-F., Riccio, A.A., and Pascal, J.M. (2014). PARP-2 and PARP-3 are selectively activated by 5' phosphorylated DNA breaks through an allosteric regulatory mechanism shared with PARP-1. *Nucleic Acids Res.* **42**, 7762–7775.
- Marsischky, G.T., Wilson, B.A., and Collier, R.J. (1995). Role of glutamic acid 988 of human poly-ADP-ribose polymerase in polymer formation. Evidence for active site similarities to the ADP-ribosylating toxins. *J. Biol. Chem.* **270**, 3247–3254.
- Mehrotra, P., Hollenbeck, A., Riley, J.P., Li, F., Patel, R.J., Akhtar, N., and Goenka, S. (2013). Poly (ADP-ribose) polymerase 14 and its enzyme activity regulates TH2 differentiation and allergic airway disease. *J. Allergy Clin. Immunol.* **131**, 521–531.e1–12.
- Menear, K.A., Adcock, C., Boulter, R., Cockcroft, X.-L., Copsey, L., Cranston, A., Dillon, K.J., Drzewiecki, J., Garman, S., Gomez, S., et al. (2008). 4-[3-(4-cyclopropanecarbonylpiperazine-1-carbonyl)-4-fluorobenzyl]-2H-phthalazin-1-one: a novel bioavailable inhibitor of poly(ADP-ribose) polymerase-1. *J. Med. Chem.* **51**, 6581–6591.
- Meyer-Ficca, M.L., Ihara, M., Bader, J.J., Leu, N.A., Beneke, S., and Meyer, R.G. (2015). Spermatid head elongation with normal nuclear shaping requires ADP-ribosyltransferase PARP11 (ARTD11) in mice. *Biol. Reprod.* **92**, 80.
- Morgan, R.K., and Cohen, M.S. (2015). A clickable aminoxy probe for monitoring cellular ADP-ribosylation. *ACS Chem. Biol.* **10**, 1778–1784.
- Morgan, R.K., Carter-O'Connell, I., and Cohen, M.S. (2015). Selective inhibition of PARP10 using a chemical genetics strategy. *Bioorg. Med. Chem. Lett.* **25**, 4770–4773.
- Peng, B., Thorsell, A.-G., Karlberg, T., Schüler, H., and Yao, S.Q. (2016). Small molecule microarray based discovery of PARP14 inhibitors. *Angew. Chem. Int. Ed.* **56**, 248–253.
- Pinto, A.F., and Schüler, H. (2015). Comparative structural analysis of the putative mono-ADP-ribosyltransferases of the ARTD/PARP family. *Curr. Top. Microbiol. Immunol.* **384**, 153–166.
- Rolli, V., O'Farrell, M., Ménissier-de Murcia, J., and de Murcia, G. (1997). Random mutagenesis of the poly(ADP-ribose) polymerase catalytic domain reveals amino acids involved in polymer branching. *Biochemistry* **36**, 12147–12154.
- Thomas, H.D., Calabrese, C.R., Batey, M.A., Canan, S., Hostomsky, Z., Kyle, S., Maegley, K.A., Newell, D.R., Skalitzy, D., Wang, L.Z., et al. (2007). Preclinical selection of a novel poly(ADP-ribose) polymerase inhibitor for clinical trial. *Mol. Cancer Ther.* **6**, 945–956.
- Thorsell, A.-G., Ekblad, T., Karlberg, T., Löw, M., Pinto, A.F., Trésaugues, L., Moche, M., Cohen, M.S., and Schüler, H. (2017). Structural basis for potency and promiscuity in poly(ADP-ribose) polymerase (PARP) and tankyrase inhibitors. *J. Med. Chem.* **60**, 1262–1271.
- Upton, K., Meyers, M., Thorsell, A.-G., Karlberg, T., Holeczek, J., Lease, R., Schey, G., Wolf, E., Lucente, A., Schüler, H., et al. (2017). Design and synthesis of potent inhibitors of the mono(ADP-ribosyl)transferase, PARP14. *Bioorg. Med. Chem. Lett.* **27**, 2907–2911.
- Venkannagari, H., Fallarero, A., Feijs, K.L.H., Lüscher, B., and Lehtiö, L. (2013). Activity-based assay for human mono-ADP-ribosyltransferases ARTD7/PARP15 and ARTD10/PARP10 aimed at screening and profiling inhibitors. *Eur. J. Pharm. Sci.* **49**, 148–156.
- Venkannagari, H., Verheugd, P., Koivunen, J., Haikarainen, T., Obaji, E., Ashok, Y., Narwal, M., Pihlajaniemi, T., Lüscher, B., and Lehtiö, L. (2016). Small-molecule chemical probe rescues cells from mono-ADP-ribosyltransferase ARTD10/PARP10-induced apoptosis and sensitizes cancer cells to DNA damage. *Cell Chem. Biol.* **23**, 1251–1260.
- Vyas, S., Matic, I., Uchima, L., Rood, J., Zaja, R., Hay, R.T., Ahel, I., and Chang, P. (2014). Family-wide analysis of poly(ADP-ribose) polymerase activity. *Nat. Commun.* **5**, 4426.
- Wahlberg, E., Karlberg, T., Kouznetsova, E., Markova, N., Macchiarulo, A., Thorsell, A.-G., Pol, E., Frostell, Å., Ekblad, T., Öncü, D., et al. (2012). Family-wide chemical profiling and structural analysis of PARP and tankyrase inhibitors. *Nat. Biotechnol.* **30**, 283–288.
- Yoneyama-Hirozane, M., Matsumoto, S.-I., Toyoda, Y., Saikatendu, K.S., Zama, Y., Yonemori, K., Oonishi, M., Ishii, T., and Kawamoto, T. (2017). Identification of PARP14 inhibitors using novel methods for detecting auto-riboseylation. *Biochem. Biophys. Res. Commun.* **486**, 626–631.

STAR★METHODS

KEY RESOURCES TABLE

REAGENT or RESOURCE	SOURCE	IDENTIFIER
Antibodies		
Polyclonal anti-GFP produced in chicken	Abcam	Cat# ab13970, RRID:AB_300798
HRP-conjugated streptavidin antibody	Jackson Immuno Research	Cat# 016-030-084; RRID:AB_2337238
Monoclonal anti-poly/mono-ADP Ribose produced in rabbit	Cell Signaling Technology	Cat# 83732S; RRID:AB_2749864
Monoclonal anti- β -Actin produced in mouse	Santa Cruz Biotechnology	Cat# sc-47778, RRID:AB_2714189
Polyclonal anti-GFP produced in rabbit	ChromoTek	Cat# PABG1; RRID:AB_2749857
pan-ADP-ribose binding reagent	Millipore	Cat# MABE1016; RRID:AB_2665466
Bacterial and Virus Strains		
<i>Escherichia coli</i> BL21 (DE3) competent cells	Millipore	Cat# 69450
Chemicals, Peptides, and Recombinant Proteins		
6-alkyne-nicotinamide adenine dinucleotide (N-6 alkyne-NAD ⁺) (Carter-O'Connell et al., 2014)	Synthesized according to published literature	Custom
Ampicillin	Fisher Scientific	Cat# BP1760-5
Bacto Tryptone	BD Biosciences	Cat# 211699
Biotin-PEG3-azide	Click chemistry tools	Cat# AZ104
Chloramphenicol	Fisher Scientific	Cat# BP904-100
Dextrose	Fisher Scientific	Cat# D16500
Drick 5'P for PARP3 activation (Langelier et al., 2014)	IDT	Custom
DMEM	Thermo-Fisher	Cat# 11965092
Formaldehyde, 37% solution	VWR	Cat# 10790-710
Glycine	Fisher Scientific	Cat# BP381-1
HEPES	Fisher Scientific	Cat# BP310-1
Hydrogen peroxide, 30%	Fisher Scientific	Cat# H325-100
Kanamycin	Fisher Scientific	Cat# BP9065
NP-40 Substitute	Fisher Scientific	Cat# 507517565
Phosphatase inhibitor cocktails 2 and 3	Sigma	Cat# P5726-1ML, Cat# P0044-1ML
Potassium phosphate dibasic	Sigma-Aldrich	Cat# P3786-500g
Potassium phosphate monobasic	Sigma-Aldrich	Cat# P9791-100G
ProLong Diamond Antifade Mountant with DAPI	Invitrogen	Cat# P36966
Strep-HRP	Fisher Scientific	Cat# NC9705430
TCEP	Fisher Scientific	Cat# PI-20490
Tris[(1-benzyl-1H-1,2,3-triazol-4-yl)methyl]amine (TBTA)	Click chemistry tools	Cat# 1061-100
Triton X-100	Fisher Scientific	Cat# BP151-500
Veliparib (ABT-888)	Selleck Chemicals	Cat# S1004
Yeast extract	Fisher Scientific	Cat# DF0127-07-1
β -mercaptoethanol	Sigma-Aldrich	Cat# M3148-100mL
Critical Commercial Assays		
QuantaRed™ Enhanced Chemifluorescent HRP Substrate	Thermo-Fisher	Cat# 15159
CalPhos mammalian transfection kit	Fischer Scientific	Cat# NC9567834
ECL HRP substrate (SuperSignal™ West Femto)	Fischer Scientific	Cat# PI34095
ECL HRP substrate (SuperSignal™ West Pico)	Fischer Scientific	Cat# PI34080
GFP-Trap magnetic beads	Chromotek	Cat# gtm-20
Lipofectamine 2000	Invitrogen	Cat# 11668027

(Continued on next page)

Continued

REAGENT or RESOURCE	SOURCE	IDENTIFIER
Lipofectamine 3000	Thermo-Fisher	Cat# L3000008
Glutathione Sepharose 4B	Fisher Scientific	Cat# 50-197-954
Ni-NTA Agarose	Qiagen	Cat# 30210
Deposited Data		
RCSB Protein Data Bank	This paper	PDB: 6FYM and 6FZM
RCSB Protein Data Bank	Wahlberg et al., 2012	PDB: 3SMI
Experimental Models: Cell Lines		
HEK 293T cells	ATCC	Cat# CRL-3216
HeLa	Gift from the Schultz lab (OHSU)	Cat# RRID:CVCL_0058
Oligonucleotides		
ATCGAGGAAAACCTGTACTTCCAATCCAATTTT CACAAAGCAGAAGAATTATTTTCT	Eurofins Genomics	Forward primer PARP11
CTCGAATTGGGATCCGTTATCCACTTCCAATT CAATGAAAGTCTATCAAGTACTCAGGAT	Eurofins Genomics	Reverse primer PARP11
TACTTCCAATCCAATGCAGTGATGGGAATCTTT GCAAATTG	Eurofins Genomics	Forward primer for PARP4
TTATCCACTTCCAATGTTATTAGTCCTTTATCTG ATCTCCAGGCAT	Eurofins Genomics	Reverse primer PARP4
Recombinant DNA		
mRuby2-Nup50-N-10	Addgene	Cat# 55908
Software and Algorithms		
GraphPad Prism	GraphPad Software Inc	https://www.graphpad.com/scientific-software/prism/
Biorad ChemiDock MP (gel imaging)	Biorad	
Image lab 4.0.1	Bio-Rad	http://www.bio-rad.com/en-us/product/image-lab-software?ID=KRE6P5E8Z
MacPymol educational v1.74	Schrodinger	https://pymol.org/2/
Mnova NMR	Mestrelab Research	http://mestrelab.com/software/mnova/nmr/
ImageJ v1.51s	ImageJ developers	https://imagej.net
Olympus fluoview v4.2a	Olympus Life Science	https://www.olympus-lifescience.com/en/software/cellsens/
Other		
96-well Histone H1 strip plate	Trevigen	Cat# 4678-096-P
96-well nickel coated plate	Thermo Scientific	Cat# 15242
Lab-Tek dishes	Fisher Scientific	Cat# 12-565-7
Microscope cover glass	Fisher Scientific	Cat# 12-545-81
Microscope slides	Thermo Scientific	Cat# 3050

CONTACT FOR REAGENT AND RESOURCE SHARING

Further information and requests for resources and reagents should be directed to and will be fulfilled by the corresponding author, Michael S. Cohen (cohenmic@ohsu.edu).

EXPERIMENTAL MODEL AND SUBJECT DETAILS

All bacterial strains used in this study are listed in the [Key Resources Table](#) with their source and genotypes. For *E. coli*, unless stated otherwise, the strains were grown in TB media supplemented with the appropriate antibiotics.

METHOD DETAILS

Cloning

cDNA encoding full length human PARP1, full length human PARP2, human PARP10 catalytic domain, human PARP15 catalytic domain, GFP-PARP11^{WT}, GFP-PARP11^{IG}, NXF1, and SRPK2 were obtained as previously described (Carter-O'Connell et al., 2014; Meyer-Ficca et al., 2015; Morgan and Cohen, 2015; Carter-O'Connell et al., 2016). cDNA encoding full length human PARP11 and cDNA encoding the human PARP4 catalytic and BRCT domains (aa1-572, PARP4_{brct-cat}) were obtained using gBlock gene fragments containing the PARP11 gene as template (IDT) and the following primers (IDT) for subsequent Gibson assembly cloning: Forward- ATCGAGGAAAACCTGTACTTCCAATCCAATTTTCACAAAGCAGAAGAATTATTTTCT, Reverse CTCGAATTCTGATCCGTTATCCACTTCCAATTCAATGAAAGTCTATCAAGTACTCAGGAT (PARP11) and forward- TACTTCCAATCCAATGCAGT GATGGGAATCTTTGCAAATTG and reverse- TTATCCACTTCCAATGTTATTAGTCCTTTATCTGATCTCCAGGCAT (PARP4_{brct-cat}). The amplified fragments were gel purified and cloned into a pET-His-SUMO-TEV LIC cloning vector (1B), a gift from Scott Gradia (Addgene plasmid # 29653) by an isothermal assembly protocol using the Gibson assembly mix (NEB). cDNA encoding the human PARP14 catalytic and WWE domains (aa1459-1801, PARP14_{cat-wwe}) was cloned into the pNIC-Bsa4 vector using standard procedures.

Expression and Purification of Human PARP1-3, PARP10_{cat}, PARP15_{cat}, and SRPK2

N-terminal hexahistidine (His₆) human PARP1, PARP2, PARP5b_{cat}, PARP10_{cat}, PARP15_{cat}, and SRPK2 were expressed as previously described (Carter-O'Connell et al., 2014; Morgan and Cohen, 2015). Greater than or equal to 90% purity was achieved for human PARP1, PARP2, PARP10_{cat}, and PARP15_{cat}. PARP3_{FL}. Greater than or equal to 70% purity was achieved for SRPK2. Protein concentration and purity were determined by comparison to an in-gel standard curve of BSA (Bio-Rad). Purity of all proteins is shown in Figure S1.

Expression and Purification of Human Full Length PARP11_{FL} and PARP4_{brct-cat}

pET-His-SUMO-TEV-PARP11_{FL} or -PARP4_{brct-cat} plasmid was transformed into Escherichia coli BL21 (DE3) competent cells (Millipore) for His₆-SUMO-PARP4/11 expression and grown on LB agar plates (with kanamycin and chloramphenicol) overnight at 37°C. A swath of cells was inoculated into a 10 mL starter culture of LB media (with 50 µg/mL kanamycin, 34 µg/mL chloramphenicol) at 225 rpm, 37°C overnight. One or more liters of terrific broth (TB) media (12 g bacto tryptone, 24 g yeast extract, 0.4% glycerol, 17 mM KH₂PO₄, 72 mM K₂HPO₄, 1% glucose, 50 µg/mL kanamycin, 34 µg/mL chloramphenicol) was inoculated with the starter culture and grown to an OD = 0.4-0.5 at 37°C, 225 rpm. Isopropyl-β-thiogalactoside, IPTG (Sigma-Aldrich) was added to 0.4 mM to induce protein expression for 2.5-3 hrs at 37°C, 225 rpm. Cells were harvested by centrifuging, resuspended in lysis buffer (20 mM HEPES, pH 7.5, 1 mM β-mercaptoethanol, 1 mM benzamidine, 0.2% NP-40, 0.2% TWEEN-20, 500 mM NaCl, 1 mM phenylmethylsulfonyl fluoride (PMSF), 8.3 mg/L DNase I (Roche)) and lysed by sonication at 0°C (Branson sonifier 450). The lysate containing the soluble protein was clarified by centrifugation (12,000g, 30 min at 4°C). PARP11 was purified in a single step using immobilized metal affinity chromatography (Ni-NTA resin, Qiagen). ~70% purity was achieved for PARP11 and ~90% purity for PARP4.

Expression and Purification of Human PARP7_{FL}

GST-PARP7_{FL} was expressed in Escherichia coli BL21 (DE3) competent cells (Millipore). Cells were first cultured in LB media overnight at 225 rpm and 37°C in an Excella® E24 Incubator (New Brunswick Scientific). Two liters of TB media (12 g bacto tryptone, 24 g yeast extract, 0.4% glycerol, 17 mM KH₂PO₄, 72 mM K₂HPO₄, 1% glucose, 100 µg/mL ampicillin, µg/mL chloramphenicol) was inoculated with the starting culture and grown to OD₆₀₀ = 1.0 at 225 rpm and 37°C. The temperature was reduced to 16°C and expression was induced by adding isopropyl β-d-thiogalactoside (IPTG) to 0.4 mM. After incubation at 16°C for 24 h, cells were harvested by centrifugation, resuspended in lysis buffer (20 mM HEPES, pH 7.5, 1 mM β-mercaptoethanol, 1 mM benzamidine, 0.2% NP-40, 0.2% TWEEN-20, 500 mM NaCl, 1 mM phenylmethylsulfonyl fluoride (PMSF), 8.3 mg/L DNase I (Roche)) at 4°C, and lysed by sonication at 0°C, and the resulting lysate was clarified by centrifugation at 12,000 G for 30 min at 4°C. PARP7_{FL} was purified in a single step using immobilized affinity chromatography (Glutathione Sepharose 4B, Fisher Scientific). Greater than or equal to 90% purity was achieved.

Expression and Purification of Human PARP14_{cat-wwe}

N-terminal His₆-PARP14_{cat-wwe} was expressed in the Escherichia coli BL21 (DE3) competent cells (Millipore). Cells were first cultured in LB media overnight at 225 rpm and 37°C in an Excella® E24 Incubator (New Brunswick Scientific). Two liters of TB media (12 g bacto tryptone, 24 g yeast extract, 0.4% glycerol, 17 mM KH₂PO₄, 72 mM K₂HPO₄, 1% glucose, 50 µg/mL kanamycin, 34 µg/mL chloramphenicol) was inoculated with the starting culture and grown to OD₆₀₀ = 1.0 at 225 rpm and 37°C. The temperature was reduced to 16°C and expression was induced by adding isopropyl β-d-thiogalactoside (IPTG) to 0.4 mM. After incubation at 16°C for 24 h, cells were harvested by centrifugation, resuspended in lysis buffer (20 mM HEPES, pH 7.5, 1 mM β-mercaptoethanol, 1 mM benzamidine, 0.2% NP-40, 0.2% TWEEN-20, 500 mM NaCl, 1 mM phenylmethylsulfonyl fluoride (PMSF), 8.3 mg/L DNase I (Roche)) at 4°C, and lysed by sonication at 0°C, and the resulting lysate was clarified by centrifugation at 12,000 G for 30 min at 4°C. PARP14_{cat-wwe} was purified in a single step using immobilized metal affinity chromatography (Ni-NTA resin, Qiagen). Greater than or equal to 90% purity was achieved.

Histone H1 Plate Assays

52 nM PARP1 or 46 nM PARP2 in pB (20 mM HEPES pH 7.5, 5 mM MgCl₂, 5 mM CaCl₂, 0.01% NP-40, 25 mM KCl, 0.5 mM TCEP, 0.1 mg/mL activated DNA (Sigma) were added to individual wells of an 96-well Histone H1 strip plate (Trevigen). Varying concentrations of each inhibitor (0–200 μM) were pre-incubated with 200 μM 6-a-NAD⁺ in pB at RT for 5–10 min, then added to the histone plate. Final reaction concentrations: 26 nM PARP1, 23 nM PARP2, 0–100 μM inhibitor, and 100 μM 6-a-NAD⁺. This reaction proceeded for 30 min at 30°C, then the plate was washed three times with 1X PBS, three times with 1X PBST (1X PBS, 0.1% Triton X-100), once with 1X PBS, then click conjugation was performed in CB (100 μM biotin-PEG3-azide, 100 μM Tris[(1-benzyl-1H-1,2,3-triazol-4-yl)methyl]amine (TBTA, Sigma), 1 mM CuSO₄, 1 mM TCEP, 1X PBS) for 30 min at RT. The plate was then washed three times with 1X PBS, three times with 1X PBST, once with 1X PBS, and then blocked with 1% milk (Carnation) in 1X PBST for 30 min at RT. The plate was then washed three times with 1X PBS, three times with 1X PBST, once with 1X PBS, and then incubated with Strep-HRP (300 ng/μL BSA, 0.05 ng/μL Strep-HRP, 1X PBS) for 30 min at RT. The plate was then washed three times with 1X PBS, three times with 1X PBST, once with 1X PBS, and then developed with QuantaRed™ Enhanced Chemifluorescent HRP Substrate (Thermo) for 30–45 s before quenching with Quanta Red Stop Solution. Fluorescence for each sample and control was read at excitation 570 nm and emission 600 nm with a Spectra Max i3 (Molecular Devices) within five min of development. Inhibitor dose response curves were fit using linear regression in Prism 7 (GraphPad™ Software). The mean IC₅₀ for each compound was calculated from at least three independent assays.

SRPK2 Plate Assays

96-well nickel coated plate (Pierce) was incubated with 350 ng His₆-tagged SRPK2 in hB (50 mM HEPES pH 7.5, 100 mM NaCl, 4 mM MgCl₂, 0.2 mM TCEP) for 60 min at RT. After extensively washing the plate, 2–600 ng (2x) of H-Y-Φ PARPs (PARP10, 11, 14, and 15) and H-Y-E PARPs (PARP3_{FL} and PARP5b_{cat}) in hB were added to individual wells of the 96-well plate. PARP3_{FL} was activated by Dnick 5'P as described previously (Langelier et al., 2014). Varying concentrations of each inhibitor (0–200 μM) were pre-incubated with 200 μM 6-a-NAD⁺ (2x) in hB at room temperature for 5–10 min, then added to the plate. This reaction proceeded for 60 min at 30°C, the plate was then washed three times with 1X PBST (1X PBS, 0.01% Tween-20), once with 1X PBS, then click conjugation was performed in CB (100 μM biotin-PEG3-azide, 100 μM Tris[(1-benzyl-1H-1,2,3-triazol-4-yl)methyl]amine (TBTA, Sigma), 1 mM CuSO₄, 1 mM TCEP, 1X PBS) for 30 min at RT. The plate was then washed three times with 1X PBST, once with 1X PBS, and then blocked with 1% milk (Carnation) in 1X PBST for 30 min at RT. The plate was then washed three times with 1X PBST, once with 1X PBS, and then incubated with Strep-HRP (300 ng/μL BSA, 0.05 ng/μL Strep-HRP, 1X PBS) for 30 min at RT. The plate was then washed three times with 1X PBST, once with 1X PBS, and then developed with QuantaRed™ Enhanced Chemifluorescent HRP Substrate (Thermo) for 30–45 s before quenching with Quanta Red Stop Solution. Fluorescence for each sample and control was read at excitation 570 nm and emission 600 nm with a Spectra Max i3 (Molecular Devices) within five min of development. Inhibitor dose response curves were fit using linear regression in Prism 7 (GraphPad™ Software). The mean IC₅₀ for each compound was calculated from at least three independent assays.

NXF1 Plate Assay

96-well nickel coated plate (Pierce) was incubated with 350 ng His₆ tagged NXF1 in hB (50 mM HEPES pH 7.5, 100 mM NaCl, 4 mM MgCl₂, 0.2 mM TCEP) for 60 min at RT. The rest of this assay was carried out according to the above procedure for SRPK2 plate assays for H-Y-Φ PARPs.

Auto-modification Plate Assay for PARP4_{brcr-cat}

96-well nickel coated plate (Pierce) was incubated with 500 ng His₆-SUMO tagged PARP4_{brcr-cat} in hB (50 mM HEPES pH 7.5, 100 mM NaCl, 4 mM MgCl₂, 0.2 mM TCEP) for 60 min at RT. After extensively washing the plate, 660 ng of PARP4_{CB} in hB was added to individual wells of the 96-well plate. Varying concentrations of each inhibitor (0–200 μM) were pre-incubated with 200 μM 6-a-NAD⁺ in hB at room temperature for 5–10 min, then added to the plate. The rest of this assay is carried according to the above procedure for SRPK2 Plate Assays for H-Y-Φ PARPs.

Auto-modification Plate Assay for PARP7_{FL}

96-well glutathione coated plate (Pierce) was incubated with 250 ng GST tagged PARP7_{FL} in hB (50 mM HEPES pH 7.5, 100 mM NaCl, 4 mM MgCl₂, 0.2 mM TCEP) for 60 min at RT. After extensively washing the plate, 100 ng of PARP7_{FL} in hB was added to individual wells of the 96-well plate. Varying concentrations of each inhibitor (0–200 μM) were pre-incubated with 200 μM 6-a-NAD⁺ in hB at room temperature for 5–10 min, then added to the plate. The rest of this assay is carried according to the above procedure for SRPK2 Plate Assays for H-Y-Φ PARPs.

Native NAD⁺ Plate Assay

96-well nickel coated plate (Pierce) was incubated with 350 ng His₆-tagged SRPK2 in hB (50 mM HEPES pH 7.5, 100 mM NaCl, 4 mM MgCl₂, 0.2 mM TCEP) for 60 min at RT. After extensively washing the plate, 2–660 ng (2x) of H-Y-Φ PARPs (PARP10, 11, 14, and 15) and H-Y-E PARPs (PARP3_{FL} and PARP5b_{cat}) in hB were added to individual wells of the 96-well plate. PARP3_{FL} was

activated by Dnck 5'P as described previously ((Langelier et al., 2014). Varying concentrations of each inhibitor (0-200 μ M) were pre-incubated with 200 μ M NAD⁺ (2x) in hB at room temperature for 5-10 min, then added to the plate. This reaction proceeded for 60 min at 30°C, the plate was then washed three times with 1X PBST (1X PBS, 0.01% Tween-20), then blocked with 1% milk (Carnation) in 1X PBST for 30 min at RT. The plate was then washed three times with 1X PBST, once with 1X PBS, and then incubated with a pan-ADP-ribose binding reagent (MABE1016, Millipore) (Gibson et al., 2017) for 30 h at RT. The plate was then washed three times with 1X PBST, once with 1X PBS, and then incubated with HRP-conjugated secondary antibodies. The plate was then washed three times with 1X PBST, once with 1X PBS, and then developed with QuantaRed™ Enhanced Chemifluorescent HRP Substrate (Thermo) for 30-45 s before quenching with Quanta Red Stop Solution. Fluorescence for each sample and control was read at excitation 570 nm and emission 600 nm with a Spectra Max i3 (Molecular Devices) within five min of development. Inhibitor dose response curves were fit using linear regression in Prism 7 (GraphPad™ Software).

PARP Immunoprecipitation auto-MARylation Activity Assay

PARP immunoprecipitation auto-MARylation activity assays were performed as previously described (Huang et al., 2016), with some modifications. HEK 293T cells were transfected with GFP-tagged PARP6, PARP7, PARP8, PARP12 and PARP16 expression plasmids (generated in house) containing an N-terminus GFP epitope. HEK 293T cells plated on 6-well plates (Greiner Bio-One) were transfected with 3.5 μ g plasmid per well using CalPhos mammalian transfection kit (Clontech). Cells were collected 24 h post-transfection and lysed in 250 μ L per well with cytosolic lysis buffer (CLB: 50mM HEPES [pH 7.4], 150 mM NaCl, 1 mM MgCl₂, 1 mM TCEP, 1% Triton X-100; complemented with complete protease inhibitors (Roche), phosphatase inhibitor cocktails 2 and 3 (Sigma), and 1 μ M veliparib, a PARP1/2-selective inhibitor). Lysates were centrifuged at 10,000 rpm for 10 min at 4°C and supernatants were transferred to new sample tubes. 40 μ L of suspended GFP-Trap magnetic bead slurry (Chromotek) were added to 1 mg protein lysates for 1 h at 4°C with constant rotation to immunoprecipitate GFP-PARPs. Following removal of supernatant, beads were washed three times with CLB, and once with PARP reaction buffer (PRB: 50 mM Tris-HCl [pH 7.5], 50 mM NaCl, 0.5 mM TCEP, 0.1% Triton X-100; complemented with complete TM protease inhibitors phosphatase inhibitor cocktails 2 and 3, and 1 μ M veliparib), for 5 min per wash, and splitting the samples into two during the last PRB wash. For the ADPr labeling, 100 μ M 6-alkyne-nicotinamide adenine dinucleotide (6-a-NAD⁺) ((Carter-O'Connell et al., 2014)) in 50 μ L PRB was added to beads and incubated for 1.5 h at 25°C/650 rpm (400 μ M of 6-a-NAD⁺ for GFP-PARP16), in the presence or absence of 30 μ M ITK7 inhibitor. Following removal of 6-a-NAD⁺, beads were washed twice with PRB and once with PBS for 5 min per wash. Click reaction mixture (1 mM CuSO₄, 1 mM TCEP, 100 μ M TBTA, 100 μ M biotin-azide; 25 μ L volume) was added to beads and incubated for 1 h at 25°C/650 rpm. Following removal of click reaction mixture, 40 μ L of 1.5X Laemmli sample buffer with 5% β -mercaptoethanol was added to beads. Samples were heated at 95°C for 5 min and supernatants were resolved by SDS-PAGE and transferred onto 0.45 μ m nitrocellulose membranes (GE healthcare bio-sciences). Membrane blots were blocked with 5% milk-TBST for 1 h at room temperature. Blots were probed for PARP6 expression with anti-GFP primary antibody (chicken polyclonal, Abcam clone ab13970, 1:5000) for 2 h at room temperature and HRP-conjugated goat anti-chicken IgG secondary antibody for 1 h at room temperature. To detect PARP6 auto-MARylation activity, blots were probed for biotinylated proteins with HRP-conjugated streptavidin antibody (Jackson ImmunoResearch, 0.4 μ g/mL) for 60 min at room temperature. ECL HRP substrate (SuperSignal™ West Pico, ThermoFisher) was added to detect protein targets by chemiluminescence. Blots were imaged for chemiluminescent signal on a ChemiDoc MP system (Bio-Rad).

GFP-PARP10 MARylation in Cells

HEK 293T cells were transfected with GFP-PARP10 using the calcium phosphate method (Clontech). 24 h post transfection, cells were treated with increasing concentrations of ITK6 (90 min) in serum-free media at 37°C. Cells were washed with PBS, and lysed (CLB: 50 mM HEPES [pH 7.4], 150 mM NaCl, 1 mM MgCl₂, 1 mM TCEP, 1% Triton X-100) with protease inhibitors (Roche). Lysates were centrifuged at 14,000 rpm for 10 min at 4°C and supernatants were transferred to a new tube with 2x Laemmli sample buffer with 5% β -mercaptoethanol. Samples were resolved by SDS-PAGE and transferred onto nitrocellulose membranes. Membrane blots were blocked with 5% milk-TBST for 60 min at RT, followed by incubation with a pan-ADP-ribose binding reagent (MABE1016, Millipore) or a chicken GFP antibody (ab13970, Abcam) for 60 min at RT, followed by incubation with HRP-conjugated secondary antibodies. Proteins were detected by chemiluminescence and imaged on a ChemiDoc MP system (Bio-Rad).

H₂O₂-stimulated H-Y-E PARP Activation

HEK 293T cells were pre-treated with the indicated concentrations of ITK7 or veliparib for 15 min at 37°C, followed by incubation with H₂O₂ (500 μ M) for an additional 15 min. Cells were washed with PBS, lysed in CLB (50 mM HEPES [pH 7.4], 150 mM NaCl, 1 mM MgCl₂, 1 mM TCEP, 1% Triton X-100), and prepared for Western blot analysis as described above.

GFP-PARP11 auto-MARylation in Cells

HeLa cells were transfected with 3 μ g of WT GFP-PARP11 using Lipofectamine 3000 (Thermo Fisher). 24 h post transfection, cells were treated with increasing concentrations of ITK7 in serum-free media at 37°C for 3 h. Cells were lysed in cytosolic lysis buffer

(CLB: 50 mM HEPES [pH 7.4], 150 mM NaCl, 1 mM MgCl₂, 1% Triton X-100) in the presence of protease inhibitors (Roche), phosphatase inhibitor cocktails 2 and 3 (Sigma), 3 μ M veliparib, 1.2 mM phenylmethylsulfonyl fluoride (Thermo Fisher), and 1mM Tris(2-carboxyethyl)phosphine hydrochloride (Thermo Scientific). Lysates were centrifuged at 10,000 rpm for 10 min at 4°C and supernatants were transferred to a new tube. Protein concentrations were determined via the Bradford Assay (Bio-Rad). Each sample was added to 4X sample buffer with 5% β -mercaptoethanol and brought to a final volume of 20 μ L. Samples were heated at 95°C for 5 min and supernatants were resolved by SDS-PAGE before being transferred onto nitrocellulose membranes (Bio-Rad). Membrane blots were blocked with 5% milk-TBST for 1 h at RT, followed by probing with a pan-ADP-ribose antibody (Cell Signaling mAb 83732, 1:1000), GFP primary antibody (ChromoTek, PABG1, 1:1000), or β -actin primary antibody (Santa Cruz Biotechnology 47778, 1:1000) for 2 h at RT. Blots were then incubated with HRP-conjugated secondary antibodies for 1 h at RT. Blots were exposed to ECL HRP substrate (SuperSignalTM West Pico PLUS, ThermoFisher) to detect protein targets by chemiluminescence and imaged on a ChemiDoc MP system (Bio-Rad).

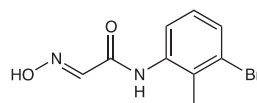
Imaging Experiments in HeLa Cells

All images were acquired on an Olympus FV1200 microscope with a PLAPON 60x/1.4NA oil objective. Live cell imaging was performed in DMEM on 37C with 5% CO₂. Cells were grown in NUNC glass bottom 8-well Lab-Tek dishes (Fisher). 25,000 cells were seeded per well, transfected using Lipofectamine2000 (Invitrogen) and imaged the next day. An image was acquired every 20 s in the GFP channel, and cells were treated with DMSO or ITK7 directly in the Lab-Tek after the acquisition of the 1st frame. For fixed samples, cells were seeded on glass coverslips (Fisher) and transfected using Lipofectamine2000 (Invitrogen). After treatments with ITK7 cells were fixed with 5% PFA for 5 min. The fixation was stopped by washing the cells with 30 mM glycine (Fisher). After PBS wash coverslips were mounted on slides with ProLong Diamond Antifade Mountant with DAPI (Invitrogen).

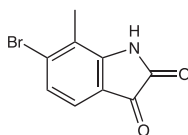
Chemical Synthesis

General

¹H NMR spectra were recorded on a Bruker DPX spectrometer at 400 MHz. Chemical shifts are reported as parts per million (ppm) downfield from an internal tetramethylsilane standard or solvent references. For air- and water-sensitive reactions, glassware was flame- or oven-dried prior to use and reactions were performed under argon. Dimethylformamide was dried using the solvent purification system manufactured by Glass Contour, Inc. (Laguna Beach, CA). All other solvents were of ACS chemical grade (Fisher Scientific) and used without further purification unless otherwise indicated. Commercially available starting reagents were used without further purification. Analytical thin-layer chromatography was performed with silica gel 60 F254 glass plates (SiliCycle). Flash column chromatography was conducted self-packed columns containing 200-400 mesh silica gel (SiliCycle) on a Combiflash Companion purification system (Teledyne ISCO). High performance liquid chromatography (HPLC) was performed on a Varian Prostar 210 (Agilent) using Polaris 5 C18-A columns (Analytical: 150 x 4.6 mm, 3 μ m; Preparative: 150 x 21.2 mm, 5 μ m) (Agilent). All final products were \geq 95% pure as assessed by analytical HPLC (mobile phase A: 0.1% formic acid (aq), mobile phase B: 0.1% formic acid in acetonitrile; flow rate = 1.0 mL/min; conditions: pre-run A = % B = 30%, 10 min A = 5% B = 95%, 12 min A = 5% B = 95%, 13 min A = 70% B = 30%; UV-Vis detection: λ_1 = 254 nm, λ_2 = 220 nm. Retention times (R_t) refer to UV = 254 nm.

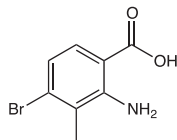


2-hydroxyimino-N-(2-methyl-3-bromo-phenyl)-acetamide. Trichloroacetaldehyde hydrate (976 mg, 5.92 mmol) and anhydrous sodium sulfate (4.5 mg, 32 mmol) were dissolved in water (15 mL), and a suspension of 3-bromo-2-methylaniline (0.67 mL, 5.38 mmol) and hydroxylamine sulfate (4.4 g, 27 mmol) in 1 N HCl (6 mL) was added. The resultant suspension of white solids in clear solution was stirred at 35°C for 1 h, then 52°C for 1.5 h, and finally 75°C for 1 h. The reaction mixture was cooled to RT and the product isolated as pale tan solids by vacuum filtration: 1.61 g (117% crude); ¹H NMR (400 MHz, Chloroform-*d*) δ 8.23 (s, 1H), 7.88 (d, J = 8.1 Hz, 1H), 7.83 (s, 1H), 7.61 (s, 1H), 7.41 (d, J = 8.0 Hz, 1H), 7.10 (t, J = 8.1 Hz, 1H), 2.39 (s, 3H).



6-bromo-7-methylindoline-2,3-dione. 2-hydroxyimino-N-(2-methyl-3-bromo-phenyl)-acetamide (1.61 g, 6.24 mmol) was added in small portions to 60°C sulfuric acid and stirred at 80°C for 1 h. The reaction mixture was cooled to RT and the product

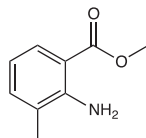
isolated as bright orange solids by vacuum filtration: 649 mg (50% crude); ^1H NMR (400 MHz, $\text{DMSO}-d_6$) δ 11.28 (s, 1H), 7.34 (d, J = 8.0 Hz, 1H), 7.28 (d, J = 8.0 Hz, 1H), 2.24 (s, 3H).



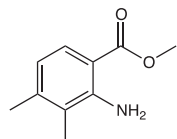
2-amino-4-bromo-3-methylbenzoic acid. 6-bromo-7-methylindoline-2,3-dione (649 mg, 2.70 mmol) dissolved in 1.3 N NaOH (135 mL) was combined with 30% H_2O_2 (7.0 mL) and water (70 mL) and stirred RT for 1 h. The reaction mixture was acidulated with 1 N HCl and the product precipitated as a white solid: 620 mg (99% crude, 45% over three steps); ^1H NMR (400 MHz, $\text{DMSO}-d_6$) δ 7.52 (d, J = 8.6 Hz, 1H), 6.78 (d, J = 8.7 Hz, 1H), 2.22 (s, 2H).

General Procedure for Synthesis of Benzoates

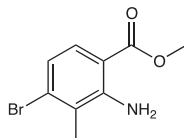
To a solution of the appropriate benzoic acid in methanol was added concentrated sulfuric acid (1% v/v) at RT. The reaction mixture was refluxed at 90°C for 18 h, monitored by TLC analysis (20% EtOAc in hexanes). Once complete the reaction mixture was poured over saturated aqueous sodium bicarbonate and separated with EtOAc. The aqueous layer was extracted with EtOAc (3x). The combined organic layers were washed with sat. aqueous sodium bicarbonate (1x), water (1x), and brine (1x), then dried over sodium sulfate and concentrated *in vacuo* to yield desired benzoate.



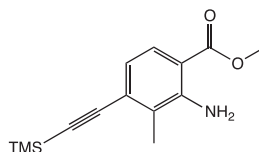
Methyl 2-amino-3-methylbenzoate. From 2-amino-3-methylbenzoic acid (500 mg, 3.3 mmol); yield 348 mg (64%); ^1H NMR (400 MHz, Chloroform- d) δ 7.77 (ddd, J = 8.1, 1.6, 0.6 Hz, 1H), 7.19 (ddq, J = 7.2, 1.7, 0.8 Hz, 1H), 6.59 (dd, J = 8.1, 7.2 Hz, 1H), 5.83 (s, 2H), 3.87 (s, 3H), 2.17 (d, J = 0.7 Hz, 3H).



Methyl 2-amino-3,4-dimethylbenzoate. From 2-amino-3,4-dimethylbenzoic acid (500 mg, 3.0 mmol); yield 400 mg (75%); ^1H NMR (400 MHz, Chloroform- d) δ 7.67 (d, J = 8.2 Hz, 1H), 6.52 (d, J = 8.3 Hz, 1H), 5.86 (s, 2H), 3.86 (s, 3H), 2.29 (s, 3H), 2.07 (s, 3H).

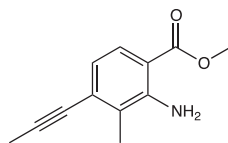


Methyl 2-amino-4-bromo-3-methylbenzoate. From 2-amino-4-bromo-3-methylbenzoic acid (620 mg, 2.69 mmol); yield 454 mg (69%); ^1H NMR (400 MHz, $\text{DMSO}-d_6$) δ 7.52 (dd, J = 8.7, 4.5 Hz, 1H), 6.85 (s, 2H), 6.83–6.79 (m, 1H), 3.79 (d, J = 1.4 Hz, 3H), 2.23 (d, J = 5.4 Hz, 3H).



Methyl 2-amino-4-ethynyl-3-methylbenzoate. TMS-acetylene (0.85 mL, 6.15 mmol) and CuI (78 mg, 0.41 mmol) were dissolved in anhydrous DMF (2 mL) in an oven dried bomb flask (15 mL capacity) and stirred under argon at RT for 30 min; solution went from clear

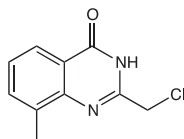
to orange. Pd(PPh₃)₂Cl₂ (144 mg, 0.205 mmol), TEA (0.36 mL, 4.10 mmol), and Methyl 2-amino-4-bromo-3-methylbenzoate (500 mg, 2.05 mmol), and additional anhydrous DMF (10 mL) were quickly added and the flask sealed under argon. The reaction proceeded at 110°C for 18 h, solution turned black over several h. The flask was cooled to RT and the reaction mixture was diluted in EtOAc (20 mL) and filtered through celite. Organics were washed with water (100 mL, 3x), and brine (100 mL, 3x). The reaction was concentrated *in vacuo* and the residue purified on a Combiflash Companion system (4 g Redisepp silica column; 0-10% EtOAc in hexanes). A mixture of the product (70%) and starting material (30%) was obtained as a yellow oil and taken on crude: 328 mg. ¹H NMR (400 MHz, DMSO-*d*₆) δ 7.53 (d, *J* = 8.6 Hz, 1H), 6.85 (s, 2H), 6.81 (dd, *J* = 8.7, 1.5 Hz, 1H), 3.79 (d, *J* = 1.5 Hz, 3H), 2.23 (d, *J* = 1.4 Hz, 3H).



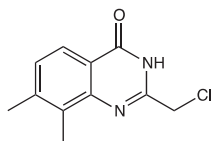
Methyl 2-amino-3-methyl-4-(prop-1-yn-1-yl)benzoate. Methyl 2-amino-3-methyl-4-bromobenzoate (200 mg, 0.99 mmol) was dissolved in anhydrous toluene and concentrated (3x 4 mL) then dried under vacuum for 1 h. The flask was evacuated and refilled with argon gas (3x), then anhydrous toluene (8 mL) was added via syringe and the solution degassed with argon 10 min. Tributyl(1-propynyl)tin (0.36 mL, 1.20 mmol) was added via syringe and the solution degassed 5 min. Palladium tetrakis (124 mg, 0.11 mmol) was added quickly and the solution degassed with argon for 3 min. The reaction mixture was refluxed at 115°C for 2.5 h. TLC analysis (10% EtOAc in hexanes) showed consumption of starting benzoate. The reaction was cooled to RT and concentrated *in vacuo*. The crude residue was purified via a Combiflash Companion system (4 g Redisepp silica column; 0-20% EtOAc in hexanes). Product was isolated as a solid: 130 mg (80%); ¹H NMR (400 MHz, Chloroform-*d*) δ 7.68 (d, *J* = 8.3 Hz, 1H), 6.71 (d, *J* = 8.4 Hz, 1H), 5.88 (s, 2H), 3.86 (s, 3H), 2.28 (s, 3H), 2.11 (s, 3H).

General Procedure for Synthesis of quinazolin-4(3H)-ones

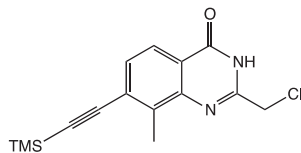
The appropriate benzoate was added to a flame-dried flask and dissolved in 4 M HCl (1,4-dioxane) under argon. To this solution was added chloroacetonitrile (3 eqv.), and the reaction mixture was refluxed under argon at 125°C overnight. Once TLC analysis revealed consumption of the starting benzoate the reaction was cooled to RT and poured over cold sat. Aqueous sodium bicarbonate and left to stand at 4°C. The desired quinazolin-4(3H)-one readily precipitated and was collected by vacuum filtration.



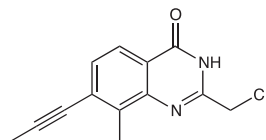
2-(chloromethyl)-8-methylquinazolin-4(3H)-one. From methyl 2-amino-3-methylbenzoate (250 mg, 1.52 mmol); yield 210 mg (48%); ¹H NMR (400 MHz, DMSO-*d*₆) δ 12.57 (s, 1H), 7.97 (d, *J* = 7.9 Hz, 1H), 7.70 (d, *J* = 7.5 Hz, 1H), 7.44 (t, *J* = 7.6 Hz, 1H), 4.56 (d, *J* = 1.3 Hz, 2H), 2.53 (d, *J* = 9.2 Hz, 3H).



2-(chloromethyl)-7,8-dimethylquinazolin-4(3H)-one. From methyl 2-amino-3,4-dimethylbenzoate (400 mg, 2.23 mmol); yield 343 mg (69%); ¹H NMR (400 MHz, Chloroform-*d*) δ 9.53 (s, 1H), 8.05 (d, *J* = 8.1 Hz, 1H), 7.33 (d, *J* = 8.1 Hz, 1H), 4.60 (s, 2H), 2.54 (s, 3H), 2.44 (s, 3H).



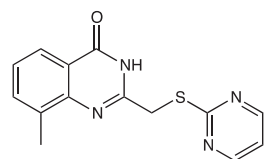
2-(chloromethyl)-7-ethynyl-8-methylquinazolin-4(3H)-one. From methyl 2-amino-4-ethynyl-3-methylbenzoate (117 mg, 0.45 mmol); yield 80 mg (77%); ^1H NMR (400 MHz, Chloroform- d) δ 10.48 (s, 1H), 8.10 – 8.05 (m, 1H), 7.55 (d, J = 8.3 Hz, 1H), 4.61 (s, 2H), 2.71 (s, 3H), 0.30 (s, 9H).



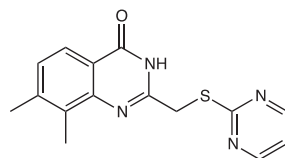
2-(chloromethyl)-8-methyl-7-(prop-1-yn-1-yl)quinazolin-4(3H)-one. From methyl 2-amino-3-methyl-4-(prop-1-yn-1-yl)benzoate (125 mg, 0.62 mmol); yield 115 mg (82%). ^1H NMR (400 MHz, DMSO- d_6) δ 12.64 (s, 1H), 7.90 (d, J = 8.2 Hz, 1H), 7.47 (d, J = 8.2 Hz, 1H), 4.56 (s, 2H), 2.62 (s, 3H), 2.16 (s, 3H).

General Procedure for Synthesis of ((pyrimidin-2-ylthio)methyl)quinazolin-4(3H)-ones

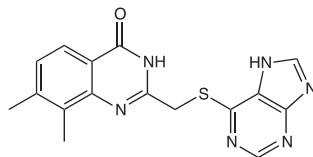
The appropriate thiol (2 eqv.) and sodium hydride (2 eqv.) were dissolved in anhydrous DMF and stirred at RT for 20 min. The appropriate quinazolin-4(3H)-one was added as a solid and the reaction mixture stirred at RT for 20 min. Once complete by TLC analysis (100% EtOAc) the reaction was poured over water, isolated, and purified as indicated.



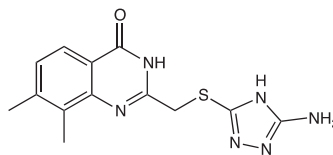
8-methyl-2-((pyrimidin-2-ylthio)methyl)quinazolin-4(3H)-one, QDR2. From 2-(chloromethyl)-8-methylquinazolin-4(3H)-one (112 mg, 0.54 mmol); reaction was concentrated *in vacuo* and product recovered as a white solid; yield 55.3 mg (36%); ^1H NMR (400 MHz, DMSO- d_6) δ 12.46 (s, 1H), 8.70 (d, J = 4.9 Hz, 2H), 7.98 – 7.94 (m, 1H), 7.70 – 7.64 (m, 1H), 7.40 (t, J = 7.6 Hz, 1H), 7.29 (t, J = 4.9 Hz, 1H), 4.48 (s, 2H), 2.48 (s, 3H); R_t : 5.81 min. HRMS m/z $[\text{M}+\text{H}]^+$ for $\text{C}_{14}\text{H}_{13}\text{N}_4\text{OS}$: 285.08046, found 285.08128.



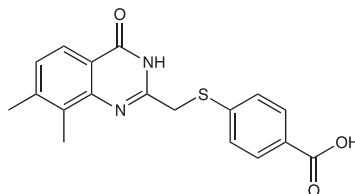
7,8-dimethyl-2-((pyrimidin-2-ylthio)methyl)quinazolin-4(3H)-one, ITK1. From 2-(chloromethyl)-7-methylquinazolin-4(3H)-one (18 mg, 0.08 mmol) and 2-mercaptopyrimidine; product precipitated as fine white solids in water; yield 15 mg (63%); ^1H NMR (400 MHz, Chloroform- d) δ 10.96 (s, 1H), 8.68 (d, J = 4.9 Hz, 2H), 8.01 (d, J = 8.0 Hz, 1H), 7.17 (t, J = 4.9 Hz, 1H), 4.33 (s, 2H), 2.56 (s, 3H), 2.43 (s, 3H); R_t : 7.58 min. HRMS m/z $[\text{M}+\text{H}]^+$ for $\text{C}_{15}\text{H}_{16}\text{N}_4\text{OS}$: 299.09611, found 299.09727.



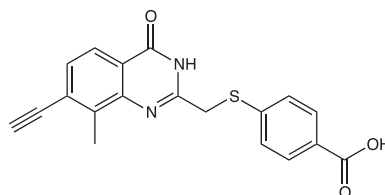
2-(((7H-purin-6-yl)thio)methyl)-7,8-dimethylquinazolin-4(3H)-one, ITK2. From 2-(chloromethyl)-7,8-dimethylquinazolin-4(3H)-one (25 mg, 0.11 mmol) and mercaptopurine; product precipitated as a white solid partition between water and EtOAc; yield 9.9 mg (27%); ^1H NMR (400 MHz, DMSO- d_6) δ 8.73 (s, 1H), 8.54 (s, 1H), 7.84 (d, J = 8.0 Hz, 1H), 7.30 (d, J = 7.7 Hz, 1H), 4.68 (s, 2H), 3.57 (d, J = 1.8 Hz, 2H), 2.39 (s, 6H); R_t : 5.84 min. HRMS m/z $[\text{M}+\text{H}]^+$ for $\text{C}_{16}\text{H}_{15}\text{N}_6\text{OS}$: 337.08661, found 337.08676.



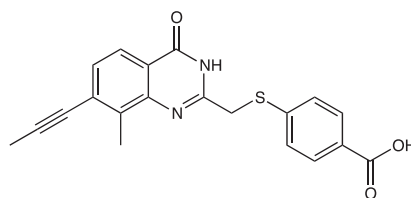
2-(((5-amino-4H-1,2,4-triazol-3-yl)thio)methyl)-7,8-dimethylquinazolin-4(3H)-one, *ITK3*. From 2-(chloromethyl)-7,8-dimethylquinazolin-4(3H)-one (25 mg, 0.11 mmol) and 3-Amino-5-mercapto-1,2,4-triazole; product precipitated as fine white solids in water; yield 25 mg (76%); ^1H NMR (400 MHz, DMSO- d_6) δ 12.28 (s, 1H), 12.09 (s, 1H), 7.84 (d, J = 8.1 Hz, 1H), 7.31 (d, J = 8.1 Hz, 1H), 6.20 (s, 2H), 4.19 (s, 2H), 2.44 (s, 3H), 2.38 (s, 3H); R_t : 4.76 min. HRMS m/z $[\text{M}-\text{H}]^+$ for $\text{C}_{13}\text{H}_{15}\text{N}_6\text{OS}$: 301.08661, found 301.08712.



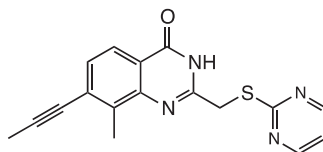
4-(((7,8-dimethyl-4-oxo-3,4-dihydroquinazolin-2-yl)methylthio)benzoic acid, *ITK4*. From 2-(chloromethyl)-7,8-dimethylquinazolin-4(3H)-one (25 mg, 0.11 mmol) and 4-mercaptobenzoic acid; product precipitated as pale yellow solids in water; yield 27 mg (73%); ^1H NMR (400 MHz, DMSO- d_6) δ 12.95 (s, 1H), 12.33 (s, 1H), 7.93 (d, J = 8.3 Hz, 1H), 7.83 (t, J = 7.2 Hz, 2H), 7.63 (d, J = 8.1 Hz, 2H), 7.29 (d, J = 8.1 Hz, 1H), 4.26 (s, 2H), 2.41 (s, 3H), 2.36 (s, 3H); R_t : 6.70 min. HRMS m/z $[\text{M}-\text{H}]^+$ for $\text{C}_{18}\text{H}_{16}\text{N}_2\text{O}_3\text{S}$: 339.07979, found 339.08030.



4-(((7-ethynyl-8-methyl-4-oxo-3,4-dihydroquinazolin-2-yl)methylthio)benzoic acid, *ITK5*. From 2-(chloromethyl)-7-ethynyl-8-methylquinazolin-4(3H)-one (10 mg, 0.043 mmol); crude product precipitated as fine white solids in water then purified by HPLC (mobile phase A: water; mobile phase B: methanol; flow rate: 20 mL/min; conditions: pre-run A = 5% B = 95%, 7 min: A = 5% B = 95%, 10 min: A = 5% B = 95%, 11 min: A = 35% B = 65%, 15 min: A = 35% B = 95; Retention time: 4.29 min; UV-Vis detection: λ_1 254 nm, λ_2 = 220 nm. Yield 6.1 mg (42%); ^1H NMR (400 MHz, DMSO- d_6) δ 12.55 (s, 1H), 7.89 (d, J = 8.2 Hz, 1H), 7.85 (d, J = 8.1 Hz, 2H), 7.62 (d, J = 8.0 Hz, 2H), 7.49 (d, J = 8.2 Hz, 1H), 4.70 (s, 1H), 4.26 (s, 2H), 2.56 (s, 3H); R_t : 8.21 min. HRMS m/z $[\text{M}-\text{H}]^+$ for $\text{C}_{19}\text{H}_{14}\text{N}_2\text{O}_3\text{S}$: 349.06414, found 349.06489.



4-(((8-methyl-4-oxo-7-(prop-1-yn-1-yl)-3,4-dihydroquinazolin-2-yl)methylthio)benzoic acid, *ITK6*. From 2-(chloromethyl)-8-methyl-7-(prop-1-yn-1-yl)quinazolin-4(3H)-one (90 mg, 0.39 mmol); product precipitated as a white solid in water; yield 80.2 mg (56%); ^1H NMR (400 MHz, DMSO- d_6) δ 12.96 (s, 1H), 12.50 (s, 1H), 7.88 – 7.82 (m, 3H), 7.62 (d, J = 8.3 Hz, 2H), 7.40 (d, J = 8.2 Hz, 1H), 4.25 (s, 3H), 2.14 (s, 3H); R_t : 8.85 min. HRMS m/z $[\text{M}+\text{H}]^+$ for $\text{C}_{20}\text{H}_{17}\text{N}_2\text{O}_3\text{S}$: 365.09544, found 365.09574.



8-methyl-7-(prop-1-yn-1-yl)-2-((pyrimidin-2-ylthio)methyl)quinazolin-4(3H)-one, *ITK7*. From 2-(chloromethyl)-8-methyl-7-(prop-1-yn-1-yl)quinazolin-4(3H)-one (15 mg, 0.06 mmol); reaction poured over water and extracted with EtOAc (3x), combined organic layers were washed with sat. aqueous sodium bicarbonate (2x), and brine (2x), then dried over sodium sulfate and concentrated in vacuo to give tan solids; yield 15.1 mg (76%); ^1H NMR (400 MHz, DMSO- d_6) δ 12.49 (s, 1H), 8.66 (d, J = 4.9 Hz, 2H), 7.87 (d, J = 8.0 Hz, 1H), 7.41 (d, J = 8.2 Hz, 1H), 7.25 (t, J = 4.9 Hz, 1H), 4.44 (s, 2H), 2.53 (s, 3H), 2.14 (s, 3H). R_t : 8.90 min. HRMS m/z $[\text{M}+\text{H}]^+$ for $\text{C}_{17}\text{H}_{15}\text{N}_4\text{O}_4\text{S}$: 323.09611, found 323.09656.

Crystallography Studies

Molecular Cloning, Protein Expression, and Purification

A synthetic cDNA fragment encoding a C-terminal segment of human PARP14 (Q460N5-6), codon optimized for expression in *Escherichia coli*, was obtained from Genscript. The fragment encoding Asp1611 – Lys1801 was inserted into pNIC-NHD (GenBank: FN677494.1). The expression construct included an N-terminal affinity tag consisting of a hexahistidine sequence separated from the protein sequence by a TEV (tobacco etch virus) protease cleavage site (sequence: MHHHHHHSSGVDLG TENLYFQSM). *Escherichia coli* BL21 (DE3) R3 pRARE cells transformed with the expression construct were used to inoculate 3 l Terrific Broth medium supplemented with 8 g/L glycerol, 50 μ g/mL kanamycin and Antifoam 204 (Sigma). Cultures were grown in Tune Air shake flasks at 37°C. When OD₆₀₀ of approximately 1.5 was reached the temperature was lowered to 18°C and protein expression was induced by addition of 0.5 mM isopropyl β -D-thiogalactopyranoside and continued for approximately 20 hrh. Cells were harvested by centrifugation at 4430 g for 10 min in a Sorvall SLC-6000 rotor. The resulting pellet was suspended in 80 mL lysis buffer (100 mM Hepes, 500 mM NaCl, 10% glycerol, 10 mM Imidazole, 0.5 mM TCEP, pH 8.0) supplemented with 1 tablet of Complete EDTA-free Protease Inhibitor (Roche Biosciences) and 8 μ L benzonase (2000 U). Suspended cells were stored at -80°C. The cells were thawed and sonicated on ice (Sonics VibraCell) at 80% amplitude, pulse: 4" on and 4" off, for a total time of 3 mins, followed by centrifugation at 49000 x g in a Sorvall SA-800 rotor, 20 mins at 4°C. The soluble fraction was decanted and filtered through a 0.45 μ m filter. Protein purification using immobilized metal affinity chromatography followed by size exclusion chromatography were carried out as previously described³. Target protein mass was verified by mass spectrometry.

Protein Crystallization

Crystals of the PARP14-ITK1 complex were obtained by the sitting-drop vapor-diffusion method in a 96-well plate (Corning) by mixing 0.2 μ L of protein at a concentration of 28 mg/ml including ITK1 dissolved in dimethyl sulfoxide (DMSO) and 0.2 μ L of reservoir solution containing 20% poly(ethylene glycol) 3350, 0.2M sodium nitrate. The plate was incubated at 20°C. After three weeks without any signs of crystal growth the plate was moved to 4°C and small rod crystals appeared within five days. Crystals were quickly soaked in cryo solution supplemented with 20 % glycerol, 300mM sodium chloride and 0.2mM ITK1 and then stored under liquid nitrogen.

Crystals of PARP14-ITK6 complex were obtained by mixing 0.1 μ L of protein at a concentration of 30 mg/ml including ITK6 dissolved in dimethyl sulfoxide (DMSO) and 0.2 μ L of reservoir solution containing 20% Poly(ethylene glycol) 3350, 0.2 M sodium nitrate and 0.1 M Bis-Tris-Propane pH 6.5. The plate was incubated at 4°C. Plate-shaped crystals appeared within seven weeks. Crystals were briefly soaked in cryo solution supplemented with 20 % Glycerol, 200 mM sodium chloride and 4 mM ITK6 and then stored under liquid nitrogen.

Crystallographic Data Collection, Phasing, and Refinement

A data set extending to 2.15 Å resolution was collected on a PARP14-ITK1 crystal at 0.92819 Å wavelength on a Dectris Pilatus 6M detector at beamline i04-1 at the Diamond Light Source (Oxfordshire, UK). The data were integrated and scaled using xia2. The crystal belonged to space group P1, and the Matthews's coefficient suggested the presence of four monomers in the asymmetric unit. The structure was solved using molecular replacement using Phaser and a previous structure of human PARP14 (PDB: 4F1L) as search model. Density for the ligand was observed in all chains and manual model building was done using COOT. Structure refinement was done using data in the interval 30.92 - 2.15 Å resolution with Buster and the progress of refinement was followed by decreasing R and R_{free} values. Grade was used to obtain ligand restraints.

A data set extending to 2.67 Å resolution was collected on the best PARP14-ITK6 crystal at 0.96858 Å wavelength on a Dectris Pilatus3 6M detector at beamline i24 at Diamond Light Source (Oxfordshire, UK). The data were integrated and scaled using XDSAPP. The crystal belonged to space group P6₂2₂, and the Matthews's coefficient suggested the presence of two monomers in the asymmetric unit. The structure was solved using molecular replacement using Phaser and the PARP14-ITK1 structure as search model. Density for the ligand was observed in both chains and manual model building was done using COOT. Structure refinement was done using Buster. In the refinement, data in the interval 49.76 - 2.67 Å resolution was used and the progress of refinement was followed by decreasing R and R_{free} values. Grade was used to obtain ligand restraints.

Summary of Crystallographic Data Collection and Refinement Statistics for PARP14-ITK1 (6FYM) Data Collection

Beam line: Diamond i04-1; wavelength (Å): 0.92819; space group: P1; unit cell dimensions (Å, Å, Å, °, °, °): 40.37, 84.04, 84.44, 119.77, 100.01, 91.44; resolution (Å): 36.7-2.15 (2.21-2.15); unique reflections: 47400 (3487); R(merge): 0.093 (0.94); completeness (%): 92.6 (91.8); redundancy: 3.6 (3.6); $\langle I \rangle / \langle \text{SIGMA} \rangle$: 9.5 (1.2); CC(1/2): 0.996 (0.513). Refinement: resolution (Å): 30.9-2.15 (2.21-2.15); R-factor (%): 19.06 (22.60); reflections used for R-factor: 36637; R-free (%): 22.39 (26.50); reflections used for R-free: 1932; r.m.s.d. bond length (Å)^a: 0.010; r.m.s.d. bond angle (°)^a: 1.0; Wilson B-factor (Å²): 41.49; Mean B-factor (Å²): 46.74; most favoured (%): 98.1; disallowed (%): 0.

Summary of Crystallographic Data Collection and Refinement Statistics for PARP14-ITK6 (6FZM) Data Collection

Beam line: Diamond i24; wavelength (Å): 0.96858; space group: P6₂2₂; unit cell dimensions (Å, Å, Å, °, °, °): 83.88, 83.88, 204.91, 90, 90, 120; resolution (Å): 49.76- 2.67 (2.83 -2.67); unique reflections: 12549 (1739); R(merge): 0.453 (1.95); completeness (%): 97.8 (86.9); redundancy: 34.8 (30.5); $\langle I \rangle / \langle \text{SIGMA} \rangle$: 10.6 (2.0); CC(1/2): 0.994 (0.769). Refinement: resolution (Å): 49.76-2.67 (2.92-2.67); R-factor (%): 23.46 (27.30); reflections used for R-factor: 12505; R-free (%): 28.88 (35.80); reflections used for R-free: 626; r.m.s.d. bond length (Å)^a: 0.010; r.m.s.d. bond angle (°)^a: 1.1; Wilson B-factor (Å²): 66.30; Mean B-factor (Å²): 51.93; most favoured (%): 90.6; disallowed (%): 0.3.

Crystallographic Data Deposition

Coordinates and structure factors for the crystal structures have been deposited in the RCSB Protein Data Bank under accession codes 6FYM and 6FZM.

QUANTIFICATION AND STATISTICAL ANALYSIS

All assays were performed at least in triplicate ($n \geq 3$). SEM were calculated in Microsoft Excel and curves were generated in Prism 7.

DATA AND SOFTWARE AVAILABILITY

All software used in this study is reported in [Method Details](#) and indicated in the [Key Resources Table](#).

Cell Chemical Biology, Volume 25

Supplemental Information

A Potent and Selective PARP11 Inhibitor

Suggests Coupling between Cellular Localization

and Catalytic Activity

Ilsa T. Kirby, Ana Kojic, Moriah R. Arnold, Ann-Gerd Thorsell, Tobias Karlberg, Anke Vermehren-Schmaedick, Raashi Sreenivasan, Carsten Schultz, Herwig Schüler, and Michael S. Cohen

A potent and selective PARP11 inhibitor suggests coupling between cellular localization and catalytic activity

Ilsa T. Kirby^{1,2}, Ana Kojic^{3,4} and Moriah R. Arnold², Ann-Gerd Thorsell⁵, Tobias Karlberg⁵, Anke Vermehren-Schmaedick², Raashi Sreenivasan², Carsten Schultz^{1,2,3}, Herwig Schöler⁵, and Michael S. Cohen^{1,2*}

¹Program in Chemical Biology, ²Department of Physiology and Pharmacology, Oregon Health & Science University, Portland, Oregon 97210, United States, ³European Molecular Biology Laboratory (EMBL), Cell Biology and Biophysics Unit, Meyerhofstrasse 1, 69117 Heidelberg, Germany, and ⁴(Candidate for) Joint PhD degree from EMBL and Heidelberg University, Faculty of Biosciences, ⁵Department of Biosciences and Nutrition (BioNut) Karolinska Institutet Hälsovägen 7c S-14157 Huddinge, Sweden.

Table of contents	Page Number
I. Figure S1-3	2
II. Table S1.....	8

Figure S1

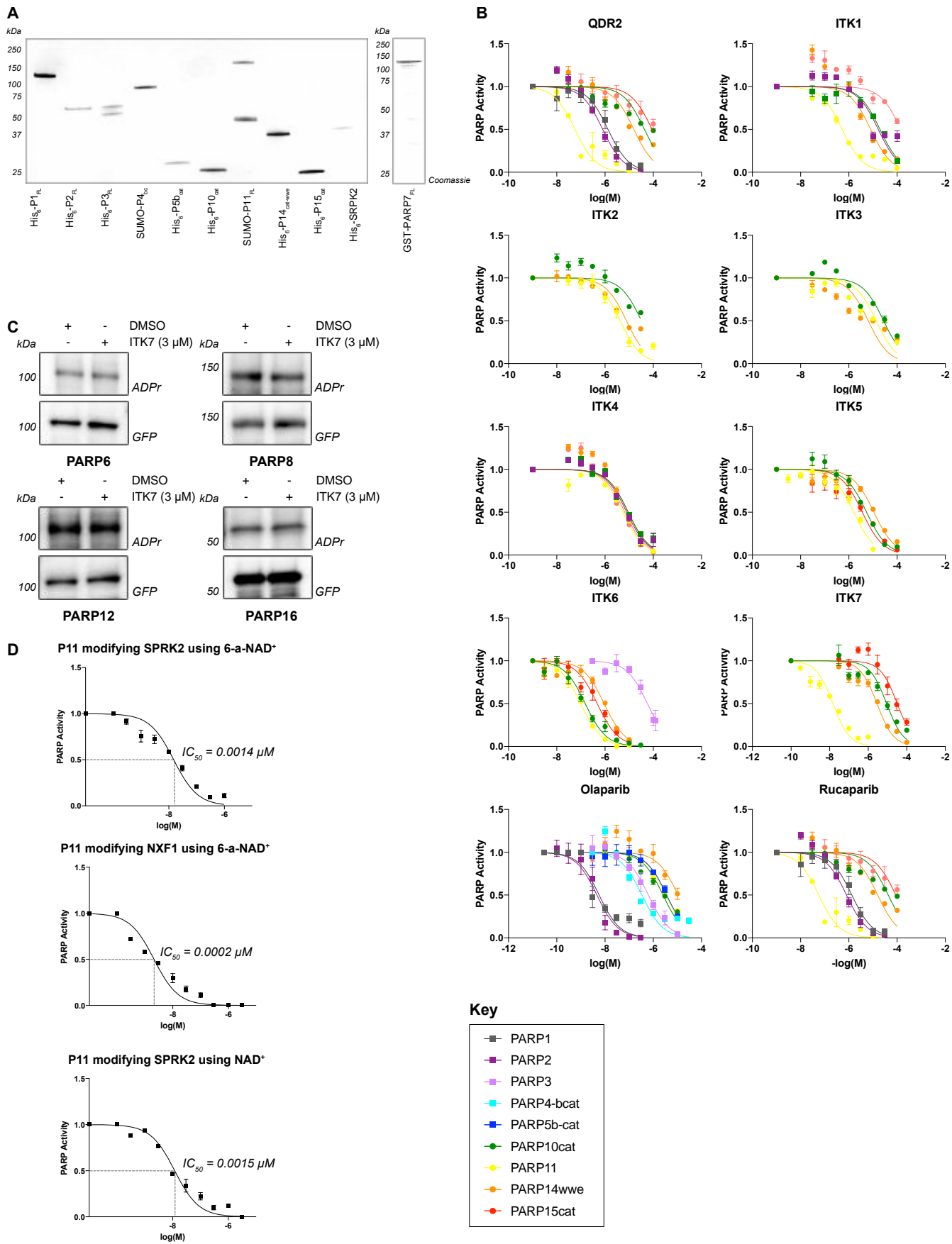


Figure S1. Related to Figure 2 and Tables S1. Family wide *in vitro* screen of QDR2, ITK1-7, olaparib and rucaparib.

(A) Recombinant PARPs used in this study. Protein samples were run on a 4-20% gradient SDS-PAGE gel (Bio-Rad) and imaged for coomassie staining on a ChemiDoc MP system (Bio-Rad).

(B) Dose response curves for QDR2 and ITK1-7, olaparib, and rucaparib against PARP1_{FL}, PARP2_{FL}, PARP3_{FL}, PARP4_{brct-cat}, PARP5_{bcat}, PARP7_{FL}, PARP10_{cat}, PARP11_{FL}, PARP14_{cat-wwe}, and PARP15_{cat} determined with *in vitro* plate assays using either SRPK2 or the PARP itself as a substrate and 6-a-NAD⁺ followed by click chemistry. Curves generated using Prism 7 (Graph Pad); error bars indicate \pm SEM from at least three replicates.

(C) HEK 293T cells transfected with GFP-PARP6, GFP-PARP8, GFP-PARP12, or GFP-PARP16 were lysed after 24 h and GFP-PARPs immunoprecipitated on magnetic beads. Immunoprecipitated PARPs were incubated with either DMSO or ITK7 (3 μ M) for 1.5 h at 25°C with 100 μ M (GFP-PARP6-12) or 400 μ M (GFP-PARP16) 6-a-NAD⁺ based on the literature K_m of NAD⁺ (Thorsell et al., 2017). Auto-MARYlation was analyzed by Western blot with an ADP-ribose (ADPr) binding reagent (uncropped blots shown below).

(D) Dose response curves for ITK7 inhibiting PARP11 mediated MARYlation of SRPK2 and NXF1 using either 6-a-NAD⁺ or native NAD⁺ in *in vitro* plate assays. Curves generated using Prism 7 (Graph Pad); error bars indicate \pm SEM from at least two replicates.

Figure S3

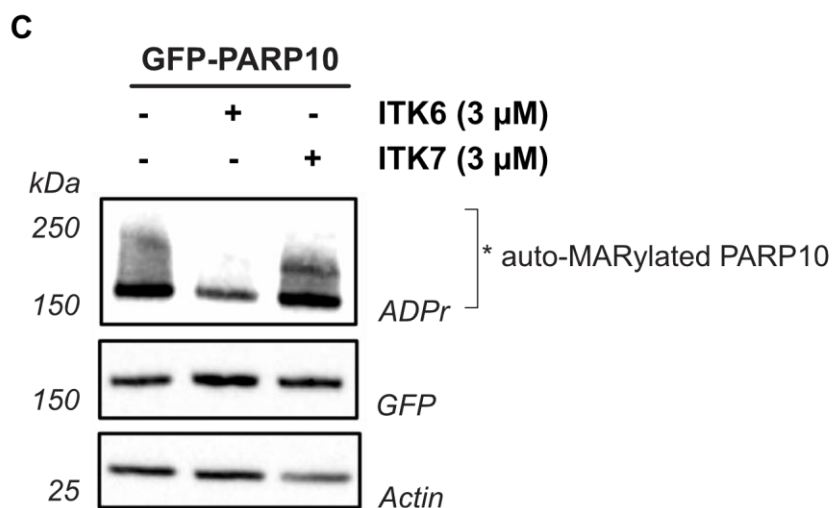
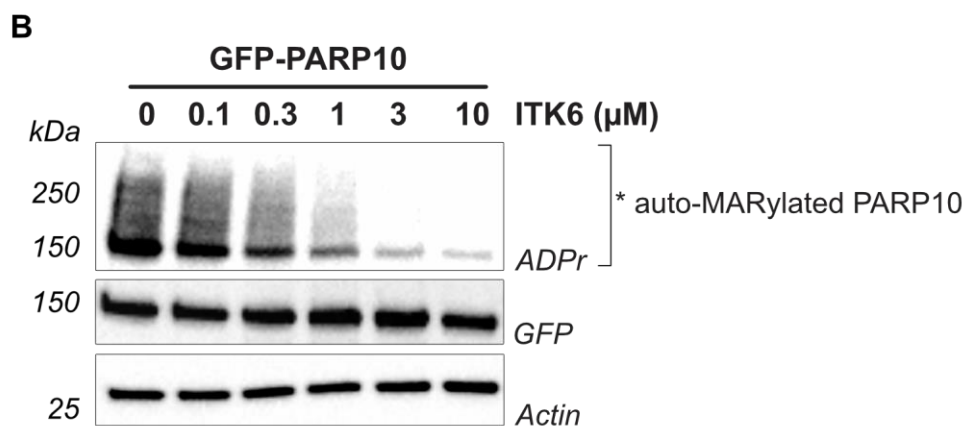
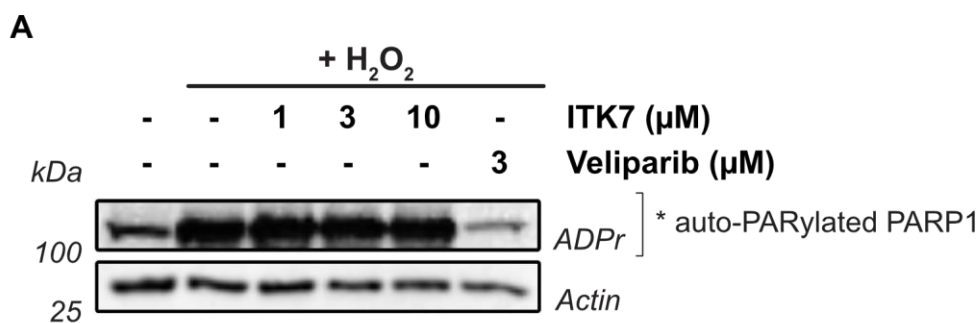


Figure S2. Related to Figure 4. ITK7 does not inhibit PARP1/2 or PARP10 in cells.

(A) ITK7 does not inhibit H₂O₂-stimulated PARP1/2 activity in cells. HEK 293T cells were stimulated with H₂O₂ (500 μM) for 15 min in the presence of DMSO, ITK7 or veliparib. As expected, veliparib, a PARP1/2-selective inhibitor, completely inhibits H₂O₂-mediated PARP1 PARylation while ITK7 has no effect. Lysates were prepared and PAR/MARylation was analyzed by Western blot with an ADP-ribose (ADPr) binding reagent. Blot was also probed with antibodies for GFP and actin. The band of interest represents auto-PARylated GFP-PARP1.

(B) ITK6, a pan-H-Y-Φ PARP inhibitor, inhibits PARP10 auto-MARylation in cells in a dose dependent manner. HEK 293T cells were transfected with GFP-PARP10. Cells were then incubated with increasing concentrations of ITK6 for 90 min. Lysates were prepared and MARylation of PARP10 was analyzed by Western.

(D) ITK6 inhibits PARP10 auto-MARylation in cells whereas ITK7 does not inhibit PARP10. HEK 293T cells were transfected with GFP-PARP10. 24 h post-transfection cells were treated with either ITK6 (3 μ M) or ITK7 (3 μ M) for 3 h. Lysates were prepared and PAR/MARylation was analyzed by Western blot with an ADP-ribose (ADPr) binding reagent.

Figure S3

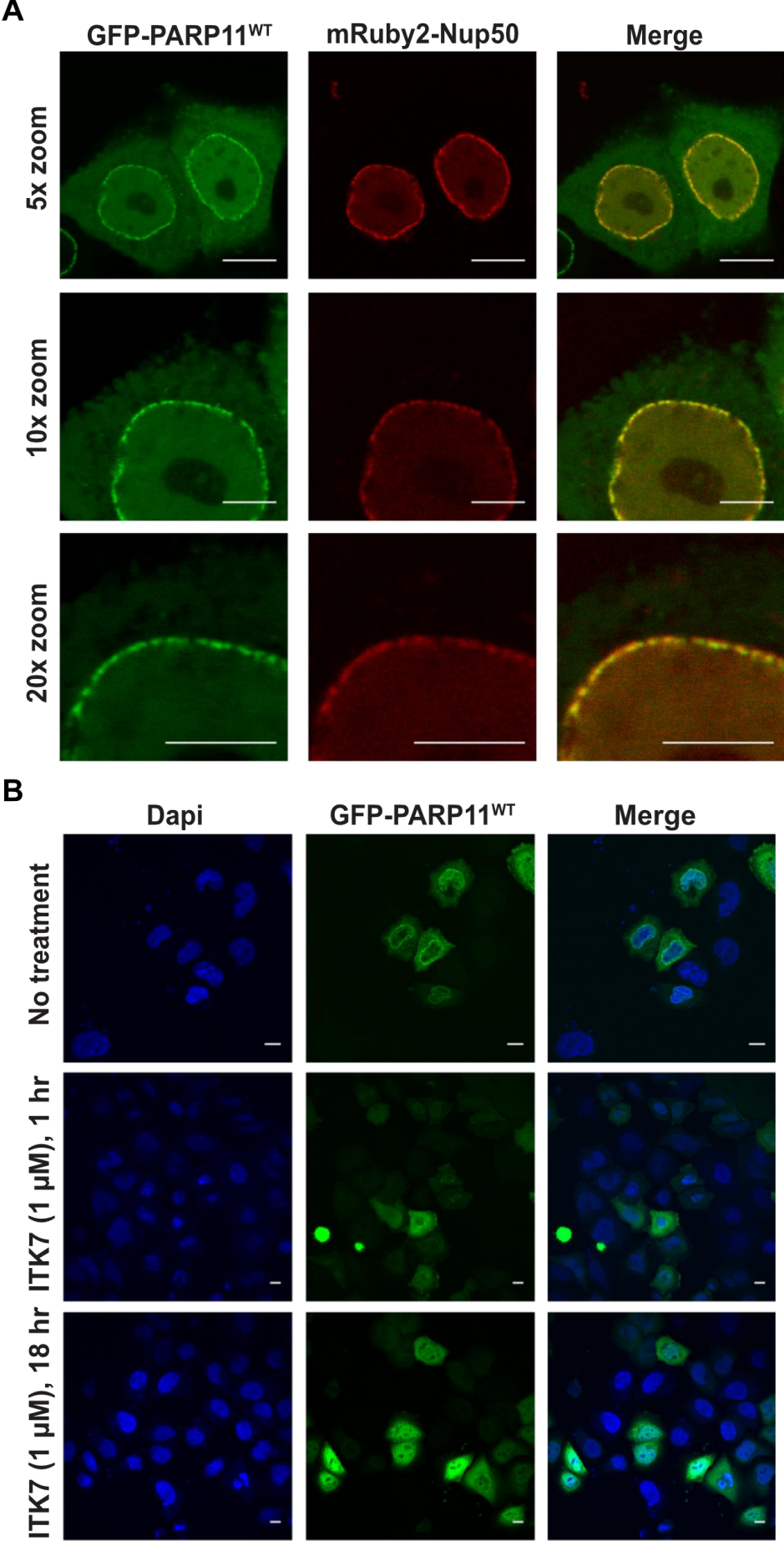
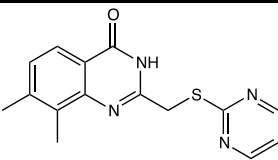
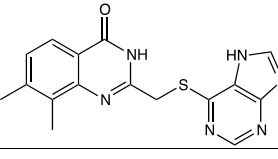
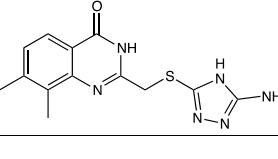
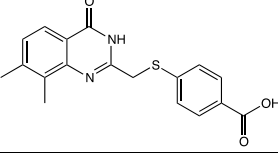


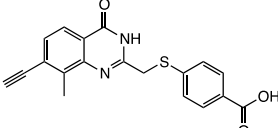
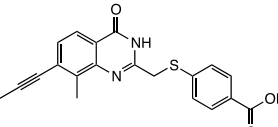
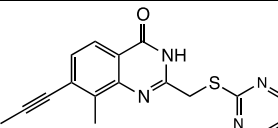
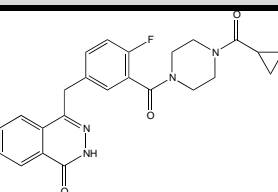
Figure S4. Related to Figure 4. GFP-PARP11 co-localizes with the nuclear pore complex (NPC) protein NUP50 and ITK7 treatment causes PARP11 to dissociate from the nuclear envelope.

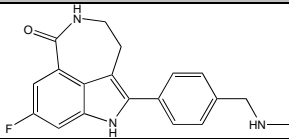
(A) GFP-PARP11 and mRuby2-Nup50 co-localize at the nuclear envelope. GFP-PARP11 and mRuby2-Nup50 were transfected in HeLa cells. Cells were grown in 8 well Lab-Tek with glass bottom. Images were taken sequentially to avoid any possible bleed through from GFP to the red channel. Images were acquired with 60x/NA 1.40 oil objective on Olympus FluoView 12000 microscope, with 5x, 10x or 20x zoom (Scale bar 10 μ m in 5x zoom, and 5 μ m in 10x and 20x zoom).

(B) ITK7 causes GFP-PARP11 to dissociate from the nuclear envelope. HeLa cells were transfected with GFP-PARP11 grown on glass cover-slips. After ITK7 (1 μ M) treatment for 1 or 18 h cells were fixed and mounted using mounting medium containing DAPI. Images were taken on the Olympus Fluoview 2000 microscope using an 60x/NA 1.40 oil objective (scale bar 10 μ m).

Table S1. Related to Figure 2 and Figure S1. *In vitro* IC₅₀ (μM) values for ITK1-7, olaparib and rucaparib; SEM from a minimum of three dose-response experiments.

ITK1	PARP1	PARP2	PARP3	PARP4 _{brct-cat}	PARP5 _{bcat}	PARP6	PARP7
	>30	17.4±3.3	>30	nt	>10	nt	nt
	PARP8	PARP10 _{cat}	PARP11	PARP12	PARP14 _{cat-wwe}	PARP15 _{cat}	PARP16
	nt	19.7±0.95	0.55±0.1 1	nt	8.55±0.80	>30	nt
ITK2	PARP1	PARP2	PARP3	PARP4 _{brct-cat}	PARP5 _{bcat}	PARP6	PARP7
	>30	>30	>30	nt	>10	nt	nt
	PARP8	PARP10 _{cat}	PARP11	PARP12	PARP14 _{cat-wwe}	PARP15 _{cat}	PARP16
	nt	32.8±3.6	4.52±1.4	nt	7.87±0.20	>30	nt
ITK3	PARP1	PARP2	PARP3	PARP4 _{brct-cat}	PARP5 _{bcat}	PARP6	PARP7
	>30	>30	>30	nt	>10	nt	nt
	PARP8	PARP10 _{cat}	PARP11	PARP12	PARP14 _{cat-wwe}	PARP15 _{cat}	PARP16
	nt	27.9±3.9	13.6±1.4	nt	6.73±1.8	>30	nt
ITK4	PARP1	PARP2	PARP3	PARP4 _{brct-cat}	PARP5 _{bcat}	PARP6	PARP7
	>30	8.46±1.40	>30	nt	>10	nt	nt
	PARP8	PARP10 _{cat}	PARP11	PARP12	PARP14 _{cat-wwe}	PARP15 _{cat}	PARP16

	nt	9.29±0.20	5.50±0.8 0	nt	8.71±0.80	6.85±0.99	nt
ITK5	PARP1	PARP2	PARP3	PARP4_{brct-cat}	PARP5_{bcat}	PARP6	PARP7
	>30	>30	>30	nt	>10	nt	nt
	PARP8	PARP10_{cat}	PARP11	PARP12	PARP14_{cat-wwe}	PARP15_{cat}	PARP16
	Nt	5.40±0.17	1.62±0.3 3	nt	10.8±0.75	4.03±0.77	nt
ITK6	PARP1	PARP2	PARP3	PARP4_{brct-cat}	PARP5_{bcat}	PARP6	PARP7
	>30	>30	>30	>30	>30	>3	24.6±0.5
	PARP8	PARP10_{cat}	PARP11	PARP12	PARP14_{cat-wwe}	PARP15_{cat}	PARP16
	>3	0.156±0.01 8	0.099±0. 016	nt	0.917±0.086	0.496±0.19	nt
ITK7	PARP1	PARP2	PARP3	PARP4_{brct-cat}	PARP5_{bcat}	PARP6	PARP7
	>30	>30	>30	>30	>30	>3	24.6±0.5
	PARP8	PARP10_{cat}	PARP11	PARP12	PARP14_{cat-wwe}	PARP15_{cat}	PARP16
	>3	9.28±1.57	0.014±0. 003	>3	2.86±0.35	>30	>3
Olaparib	PARP1	PARP2	PARP3	PARP4_{brct-cat}	PARP5_{bcat}	PARP6	PARP7
	0.025± 0.002	0.007±0.00 03	0.083±0. 037	0.241±0.015	0.211±0.081	nt	nt
	PARP8	PARP10_{cat}	PARP11	PARP12	PARP14_{cat-wwe}	PARP15_{cat}	PARP16

	>3	4.5±0.3	>10	~10	>10	>10	~5
Rucaparib	PARP1	PARP2	PARP3	PARP4_{brct-cat}	PARP5_{bcat}	PARP6	PARP7
	0.008± 0.002	0.005±0.00 1	0.72±0.3 7	0.450±0.101	3.6±0.3	<i>nt</i>	<i>nt</i>
	PARP8	PARP10_{cat}	PARP11	PARP12	PARP14_{cat-wwe}	PARP15_{cat}	PARP16
	<i>nt</i>	2.5±0.2	3.4±0.5	~7	>10	>10	<i>n.i.</i>